Montanuniversität Leoben

Contact modeling of CVD coatings for cutting tools

Diploma Thesis

by

Elisabeth Brettner

Leoben, June 2010

This work has been carried out in corporation with CERATIZIT Austria G.m.b.H., Ceratizit Luxembourg S.á.r.l. and Materials Center Leoben Forschung G.m.b.H., at the Department of Physical Metallurgy and Materials Testing, Montanuniversität Leoben.

This thesis is carried out with the financial support of the Austrian Federal Government (in particular the Federal Ministry for traffic, innovation and technology and the Federal Ministry for economics, family and youth) as well as the country Styria, represented by the Austrian Forschungsförderungsgesellschaft mbH and the styrian Wirtschaftsförderungsgesellschaft mbH, in the framework of the from Materials Center Leoben Forschung GmbH carried out K2 Centre for “Materials, Processing and Product Engineering” within the Austrian COMET competence center program.

Affidavit

I declare in lieu of oath, that I wrote this thesis and performed the associated research by my self, using only literature cited in this volume.

Leoben, June 2010

Elisabeth Brettner

Acknowledgements

I would like to thank Univ. Prof. DI Dr. Helmut Clemens, Head of the Department of Physical Metallurgy and Materials Testing, for giving me the opportunity to perform this work at his institute at the University of Leoben.

My sincerest gratitude appertain ao. Univ. Prof. DI Dr. Christian Mitterer, Head of the Thin Film Group at the Department of Physical Metallurgy and Materials Testing in Leoben, for his kindness, his patience and his valuable support and supervision all the time.

I am grateful to ao. Univ. Prof. Reinhold Ebner, Managing Director of the Materials Center Leoben (MCL), who assigned me to this project and to all coworkers at the Materials Center Leoben.

I would like to express my thanks to DI Dr. Martin Kathrein, Ceratizit Austria in Reutte, for his support and the possibility to get an insight into research and production activities.

Furthermore, I want to express my gratitude to DI Christoph Czettl for the backup and assistance during this thesis, for his endless patience and for motivating me to do this work.

I would also like to thank all my colleagues of the Thin film Group, especially to DI Dr. Claudia Walter and Dr. Rostislav Daniel.

Finally, very special thanks appertain to my family for their everlasting support in every sense throughout all my life. Without their encouragement it would have never been possible to do this study.

Contents

1 Introduction 1
2 Theoretical background 2
2.1 Chemical vapor deposition 2
2.1.1 Material selection 2
2.1.2 Substrate and coating system 4
2.2 Residual stress 9
2.2.1 Stress classification by dimension 9
2.2.2 Origin of residual stresses 10
2.2.3 Determination and modification of the stress state 12
2.3 Nanoindentation testing and evaluation 14
2.4 Modeling 17
2.4.1 Contact mechanics 17
2.4.2 Software package ELASTICA 20
3 Experimental and modeling details 21
3.1 Nanoindentation measurements 21
3.2 Determination of cutting force and contact area 22
3.3 XRD analysis 23
3.4 Modeling with ELASTICA 23
4 Results and discussion 24
4.1 Input data for modeling 25
4.2 Substrate WC-Co 26
4.3 Hypothetical layer system 28
4.3.1 Substrate with TiN 30
4.3.2 Substrate with TiCN 32
4.3.3 Substrate with κ-Al_2O_3 33
4.3.4 Substrate with α-Al_2O_3 35
4.3.5 Substrate with internally stressed α-Al_2O_3 layer 36
4.4 Reduced layer system 41
4.4.1 Three layer system with α-Al_2O_3 on top 41
4.4.2 Three layer system with κ-Al_2O_3 on top 43
4.4.3 Reduced three layer system with internally stressed α-Al_2O_3 45
5 Summary, conclusions and outlook 50
5.1 Summary 50
5.2 Conclusions 51
5.3 Outlook 52
6 References I

1 Introduction

Because of mechanical contacts, which take place in dynamic systems, engineers have to protect surfaces from wear by providing sufficient reliability and durability. The last decades have shown that thin hard coatings are able to fulfill these requirements. It is possible to increase lifetime and wear resistance of critical components by using thin film coatings with suitable properties [1].

The growing need of contemporary technical and mechanical applications leads the engineers to design suitable film substrate combinations. Up to the last decade, these investigations are mainly based on empirical approaches were results of hardness, scratch, wear or other tests were used. This is a time consuming process and to cut this down, computer simulations have been applied with the advantage that experimental efforts are reduced and results are obtained within comparably short time [1-2].

The objective of this thesis is to explore coating architectures for cutting applications with respect to mechanical failure. The substrate materials of interest are cemented carbide inserts. These inserts are frequently coated by chemical vapor deposition (CVD). Often, the coatings consist basically of a Ti(C, N) base layer, a bonding layer and α- or κ-aluminum oxide.

The coating is a compound of different layers with different structure and properties like thickness, thermal expansion coefficient, hardness and elastic modulus. Each layer has a different function, like good adhesion to the substrate, wear resistance, toughness or oxidation resistance. Thus, to get a high-performance coating-substrate system it is necessary to evaluate the influence of the different properties. This can be done by Finite Element methods (FEM) or with analytical models. The approach used in this work is based on a combination of indentation experiments to determine mechanical properties like elastic modulus and hardness of the coatings, and the commercial analytical simulation package ELASTICA to calculate the stress imposed by external mechanical loads within the individual layers.

The internal stress profile is an indicator for mechanical failure and so it is important to determine the stress maxima within the layers [1]. The aim of this work is to evaluate the suitability of this approach based on nanoindentation experiments and ELASTICA simulation to determine critical areas in CVD hard coating systems of relevance for cutting application.

2 Theoretical background

2.1 Chemical vapor deposition

The application of thin, wear resistant coatings deposited by CVD is one of the most important developments for the hard metal industry in the last decades [3].
The term CVD covers processes in a thermally activated environment where a stable solid deposit is formed by dissociation and/or chemical reaction of the gaseous reactants. There are a lot of variants of CVD methods. The method used for this work was the thermally activated LP-CVD (low pressure) where the chemical reactions are initiated by thermal energy and inorganic chemical precursors were used. The deposition takes place at temperatures between 800 – 1000 °C and a pressure of 50 – 900 mbar [4].
High hardness, especially hot hardness, good adhesion between coating-substrate and between individual layers in a multilayer system, chemical stability, good oxidation resistance and low thermal conductivity are the basic requirements for wear resistant coatings for cutting tools [5]. Thus, the variety of suitable materials for a highly productive tool coating is limited.

2.1.1 Material selection

A huge number of hard materials are known, and so it is not easy to find the most suitable coating material for particular needs. Therefore, it is important to have some criteria for the selection which is, with regard to the complex requirements for the composite substrate/layer, challenging. Figure 2.1 gives an overview about important criteria for the combination of substrate and layer. In this setup, three different zones can be distinguished and each of them has to fulfill different requirements [6]. With beginning on top, the *layer surface* is the first zone. In this zone the interaction tendency of the layer material with a work piece or the environment is important. The second zone is the *layer material* where properties like strength, hardness, internal stress, fracture toughness, thermal stability and thermal conductivity are determined by its composition and microstructure. The last zone is the interface between substrate and layer, where adherence, interactions (reactions) between substrate and layer and strains which occur because of thermal expansion misfits are the most important criteria. One challenge in material selection is that all the desired properties cannot be achieved coeval; for example an increasing hardness and strength are mostly accompanied by decreasing toughness and adherence. The coating material properties are mainly influenced by three factors: First, the constitution of the system (substrate, layer, substrate/layer interface); second, the coating deposition parameters like coating process and layer thickness

and third the result of both, the microstructure of the coating (density, phases, grain sizes, boundaries, orientation).

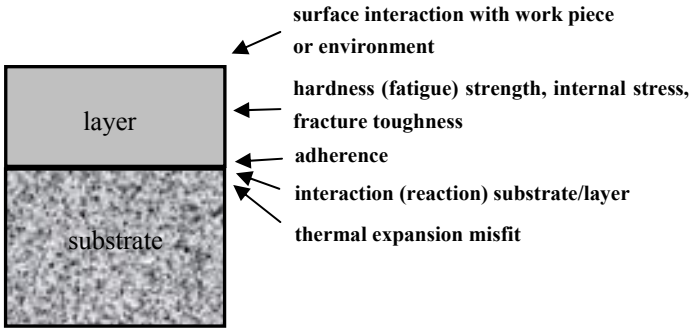

Fig. 2.1: Important criteria for material selection [6].

According to their chemical bonding character, one can divide hard materials for coatings in three different groups [6]. One group are the metallic ones, i.e. borides, nitrides and carbides of the transition metals, representing the most important coating substances. The second group comprises the covalent hard materials, for example borides, nitrides and carbides of Al, Si and B. The ionic (ceramic) hard materials are the last group which include the oxides of Al, Zr, Ti, and Be. This group is particularly suitable for the outermost layer of the coating because of its high stability and low interaction tendency. A comparison of all groups yields the conclusion that an optimum wear resistance can only be achieved by multiphase or multilayer coatings. In such systems the interface constitution is very important taking into account the complex requirements in the hard material system. Figure 2.2 shows the three different types of interfaces in multiphase coatings, which are coherent or partially coherent interfaces with a *boundary phase* and interaction free interfaces.

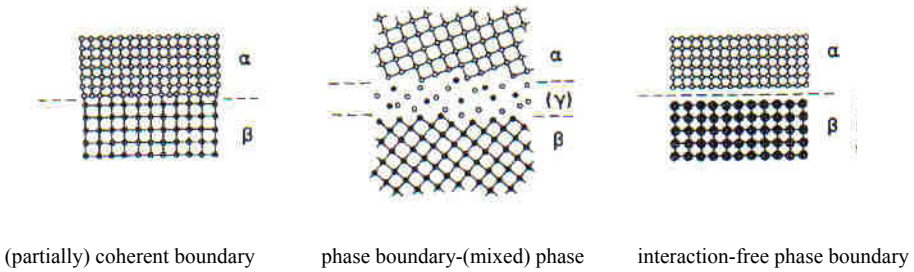

Fig. 2.2: Different natures of interfaces in multiphase coatings or at the substrate/layer interface [6].

To obtain an optimum adherence low-energy interfaces are necessary, which can be observed in metallic hard materials. They form coherent or semi-coherent interfaces with metals or other metallic hard materials, for example in TiC/TiB_2 [6]. Intermediate regions of variable

composition can often be formed at interfaces between metallic and ionic hard materials like TiC/Al_2O_3. An example for an interaction-free interface is B_4C/Al_2O_3, an interface between covalent hard materials. The consequence is a low strength of the interface between the phases and thus low adhesion.

There are fundamental relations between the position of the coating material components in the Periodic Table of elements and the properties which can be used for optimizing the material selection. Metallic hard materials play a significant role in coating industry. The metallic bonding and also the localized metal-nonmetal bonds are responsible for their beneficial properties. From the fourth (TiC) to the sixth (WC) group of the transition metal carbides, the amount of metallic bonding increases. The consequences are changing properties. For example, from group IV to group V transition metal carbides a decrease of room-temperature hardness can be observed, an increase of fracture toughness, and also an increase of solubility in Fe, Co, and Ni.

There are some ways to control the properties of the metallic hard compound, for example by changing the stoichiometry of the components which means the adjustment of a certain nonmetal-to-metal ratio. Another one is the coating process itself, which often allows adjusting specific phase orientations, thus avoiding anisotropy.

With respect to the special characteristics of the different hard materials, it is possible to design coatings with good adherence between the coating and the substrate, with high hardness and strength and an outermost layer which reduces friction, adhesion and reactivity [6]. With respect to all the requirements mentioned above, an often used concept for a protective coating on cemented carbide cutting tools is a multilayer coating containing a combination of TiN, TiC, Ti(C, N) and Al_2O_3 layers [4].

2.1.2 Substrate and coating system

The application of cemented carbide tools ranges from rock drilling to metal cutting because of their wide range of properties due to the possible compositional and micro-structural modifications. Thus, cemented carbides with special mechanical properties optimized for the given application can be produced. In metal cutting, the performance of cemented carbides can be improved by coatings of TiC, TiN, Ti(C, N) and Al_2O_3. Figure 2.3 shows a scanning electron microscopy (SEM) image of the layer system investigated in this work with WC-Co as cemented carbide. The materials used are explained in detail in the following sections.

Cemented carbide

Cemented carbides consist typically of WC and a Co-rich binder phase. The wear resistance of the straight WC-Co alloys can be improved by adding a third phase of cubic transition

metal carbides, like Ti-, Ta-, or Nb-C which are usually referred to as γ-phase. But the main component in most of the commercial cemented carbides is WC. Table 2.1 shows some characteristics and properties of WC. The binder phase, a Co-rich alloy with C and W in solid solution, has usually a much lower volume fraction than that of WC. The modification of the Co binder phase in cemented carbides is face centered cubic (f.c.c.) [7].

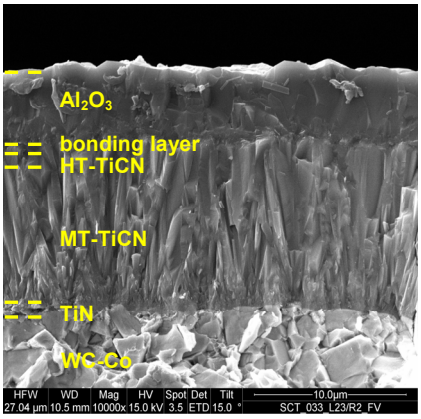

Fig. 2.3: SEM cross section image of the investigated layer system.

Tab. 2.1: Summary of characteristics and properties of the materials investigated within this thesis (test temperature is 20 °C unless otherwise stated) [8].

	WC	TiC	TiN	Al_2O_3
Structure	hexagonal	face centered cubic	face centered cubic	rhombohedral
Lattice Parameter [nm]	a 0.2907; c 0.2837	0.4328	0.424	0.513
Composition	α-$WC_{0.98}WC_{1.00}$	$TiC_{0.47}$ to $TiC_{0.99}$	$TiN_{0.6}$ to $TiN_{1.1}$	Al_2O_3
Molecular Weight [g/mol]	195.86	59.91	64.95	101.96
Color	gray	silver gray	gold	white
X-ray Density [g/cm^3]	15.8	4.91	5.4	3.965
Melting Point [°C]	2870 (decomposes incongruently)	3067	2950	2015
Specific Heat (C_p) [J/mole*K]	39.8	33.8	33.74	-
Heat of Formation at 298K [KJ/g-atom metal]	37.7	184.6	338	-
Thermal Conductivity (K) [W/m°C]	63	21	19.2	25-29
Thermal Expansion [/°C] *10^{-6}	a 5.2; c 7.3	7.4	9.35	7-8.3
Hardness [GPa]	22 (little change at high temperatures)	28-35	18-21	18.73
Modulus of Elasticity [GPa]	620-720	410-510	251	378
Shear Modulus [GPa]	262	186	-	-
Bulk Modulus [GPa]	-	240-390	-	-
Poisson's Ratio	0.18	0.191	-	-
Transverse Rupture Strength [MPa]	550	240-390	-	421

There is an inverse relationship between the amount of W in solid solution and the C content of the binder phase. An increase in the C content results in a decreased amount of dissolved W and vice versa. If there is a deficiency of C in the binder phase, the brittle η phase can be formed. On the other hand, an excess of C leads to the formation of C porosity. Both are very

destructive for the mechanical properties of cemented carbides and also for coating adhesion, because there the interfacial structure and its strength is of vital importance [7].

Titanium carbide

TiC is an important industrial material of unusual hardness with high strength and rigidity and has also a good wear resistance. Its properties are summarized in Table 2.1 [8]. The first commercial single CVD TiC coating has been introduced in 1969. The classical overall reaction where TiC is formed is shown in Equation 2.1.

$$TiCl_4\,(g) + CH_4\,(g) + H_2\,(g) \longrightarrow TiC\,(s) + 4HCl\,(g) + H_2\,(g) \qquad (2.1)$$

Most of the C needed for the formation of TiC originates at the beginning of the coating process from the cemented carbide itself. The result is a decarburization of the interfacial part of the substrate which leads to the formation of the brittle η carbide Co_6W_6C. Additionally, interfacial porosity in the substrate can occur because of diffusion processes. These phenomenons are in many applications destructive for the cutting properties of coated cemented carbides [5, 7]. To avoid the formation of the η carbide, TiN as innermost layer instead of TiC has been introduced.

Titanium nitride

TiN is formed in a heterogeneous chemical reaction on the surface of the cemented carbide, where the layer forming components originate from the gas phase. Equation 2.2 shows this reaction.

$$TiCl_4\,(g) + \tfrac{1}{2}\,N_2\,(g) + 2H_2\,(g) \longrightarrow TiN\,(s) + 4HCl\,(g) \qquad (2.2)$$

The properties of TiN are summarized in Table 2.1. The deposition temperature of TiN is slightly lower than that of TiC. TiN is in general used as an intermediate layer between cemented carbides and MTCVD (moderate temperature) Ti(C, N) coatings. A TiN layer avoids the diffusion of the carbon from the substrate to the Ti(C, N) layer. It is an excellent diffusion barrier. Consequently, the embrittlement because of the decarburization of the cemented carbide, due to formation of the η phase, can be avoided. A CVD TiN layer is, in the absence of C, typically composed of columnar grains. The crystal orientation can be controlled by the deposition pressure, where higher pressures improve its efficiency as a diffusion barrier [5, 8-9].

Titanium carbonitride

In Ti(C, N) the wear properties of TiC and the low friction as well as oxidation and chemical resistance of TiN are combined. Equation 2.3 shows the simplified forming reaction which uses the $TiCl_4$ - CH_4 - N_2 system for deposition. This corresponds to the conventional CVD process which takes place at a temperature of approximately 1000 °C.

$$TiCl_4\,(g) + xCH_4\,(g) + \tfrac{1}{2}(1\text{-}x)\,N_2\,(g) + 2(1\text{-}x)\,H_2\,(g) \longrightarrow TiC_xN_{1\text{-}x}\,(s) + 4HCl\,(g) \qquad (2.3)$$

Today, the almost exclusively used process instead of the high temperature one is the lower temperature MTCVD process which takes place at a typical deposition temperature of 800 – 900 °C and uses acetonitrile (CH_3CN) as precursor. The MTCVD Ti(C, N) is formed according to the overall reaction shown in Equation 2.4.

$$TiCl_4\,(g) + CH_3CN\,(g) + 2\tfrac{1}{2}H_2\,(g) \longrightarrow Ti(C, N)\,(s) + CH_4\,(g) + 4HCl\,(g) \qquad (2.4)$$

Due to the use of acetonitrile as precursor, the deposition of dense coatings with homogenous thickness at a reasonable growth rate is possible. Decarburization of the cemented carbide substrates during the deposition process can be reduced and thus the formation of the brittle η phase can be avoided because of the lower deposition temperature in combination with the more reactive precursors. The results are lower tensile thermal stresses in the coating layer, and an increasing toughness compared to conventional coatings.
Ti(C, N) coatings deposited by MTCVD show pronounced columnar grains with a preferred (112) growth orientation. As a consequence, the columnar grains are twinned along the growth direction with (111) twin related domains. The surfaces of these coatings are dominated by relatively large facets, which results in a rough surface. In contrast, the coatings deposited by conventional CVD have a smooth surface with small equiaxed crystals.
Nevertheless, the advantages of the MTCVD Ti(C, N) with lower tensile stress and higher toughness have fostered the replacement of the conventional CVD Ti(C, N) coatings as first intermediate layer, but it is also possible to deposit both systems in sequence [5, 8, 10].

Alumina and its polymorphs

For many applications it has been shown that alumina is the ideal layer material because of its high hot hardness, excellent chemical stability and its low thermal conductivity. For the underlayer and the substrate it acts like a thermal barrier. Further characteristic properties are shown in Table 2.1. Equation 2.5 shows a common reaction for the deposition of Al_2O_3. It is a complex reaction which includes a homogenous gas-phase reaction and heterogeneous surface reactions.

$$2AlCl_3\,(g) + 3CO_2\,(g) + 3H_2\,(g) \longrightarrow Al_2O_3\,(s) + 3CO\,(g) + 6HCl\,(g) \qquad (2.5)$$

The deposition of alumina is carried out at temperatures of 900 - 1000 °C. Historically, first coatings had to be kept relatively thin, but later it has been found that doping with H_2S enables the deposition of thicker (5 - 10 µm) Al_2O_3 coatings with acceptable uniformity [5].
Many metastable polymorphs of Al_2O_3, like κ, γ, η, δ, θ, χ are known additionally to the stable α-Al_2O_3. Two metastable alumina modifications, i.e. κ and γ, can be deposited by CVD in a controlled way additionally to the stable one. Figure 2.4 shows a SEM cross section of the two forms α and κ, which are of interest in this work.

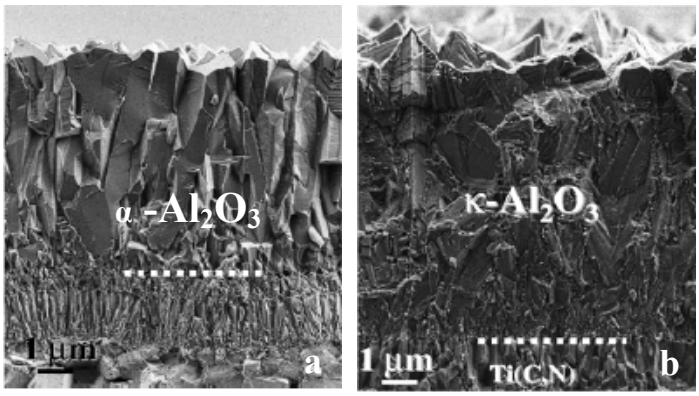

Fig. 2.4: SEM cross section of α-Al_2O_3 (a) and κ-Al_2O_3 (b) on Ti(C, N) underlayers [11].

The structure of α-Al_2O_3 belongs to the trigonal crystal system with a rhombohedrally centered hexagonal lattice. It has an …ABAB… stacking sequence of almost close-packed oxygen ions along the c-axis. κ-Al_2O_3 has a primitive orthorhombic crystal structure with an …ABAC… stacking sequence of almost close-packed oxygen ion planes [5, 11-12].
It is not possible to deposit a CVD Al_2O_3 coating as the first layer on the cemented carbide because of its poor nucleation to this substrate [13]. Alumina is usually grown on Ti(C, N) underlayers which favor the nucleation of κ-Al_2O_3. The nucleation of α-Al_2O_3 can be achieved by oxidizing treatments of the Ti(C, N) layer [12].
As mentioned above, κ-Al_2O_3 is metastable. Metastable modifications may transform to the stable α-phase during the deposition process, post-deposition heat treatment as well as during metal cutting, especially at high cutting speeds. Because of this transformation, cracking of the coating due to the volume change can occur. The adhesion of the κ-Al_2O_3 will deteriorate and eventually the coating will fail because of this volume contraction. κ-Al_2O_3 transforms directly to the stable α-Al_2O_3 at temperatures above 1000 °C [5, 11-12]. Ruppi et al. investigated α- and κ-Al_2O_3 coatings and identified their structure to be composed of columnar grains where the κ-Al_2O_3 shows only a slightly smaller grain size than the as-grown α-Al_2O_3. The transformed κ-Al_2O_3 ("α-Al_2O_3") exhibits the largest grain size and is composed of nearly equiaxed grains. The structure of κ-Al_2O_3 is dominated by planar twin- related faults

and no dislocations or pores could be found. In contrast, "α-Al_2O_3" reveals a high defect density additionally to dislocations and porosity in the form of voids and cracks. The as-grown α-Al_2O_3 shows columnar and defect-free grains elongated along the growth direction. Determination of hardness and elastic modulus indicates that the transformed κ-Al_2O_3 exhibits a lower hardness and modulus than the as-grown α-Al_2O_3 because of its high defect density and the κ-Al_2O_3 phase shows the lowest hardness and modulus.
Despite of this fact, the metastable κ-Al_2O_3 phase is frequently used as wear resistant coating on cemented carbide cutting tools [11] .

2.2 Residual stress

In 200 B.C. thick bronze discs which were flat and polished on one side, and had a relief cast on the other side, where manufactured by Chinese artisans. They were heated and quenched and by illuminating such a "magic mirror" on its flat face, the reflection shows the pattern of the relief on the other side of the disc. The reason was the occurred distortions on the flat side due to the different cooling rates of the sections of various thicknesses. These distortions lead to the imitation of the pattern of the relief. It is assumed that this was the first deliberate use of residual stress and strain [14].

2.2.1 Stress classification by dimension

One definition of residual stress was made by Toshio Mura. He defines residual stresses as the "self-equilibration internal stresses existing in a free body which has no external forces or constraints acting on its boundary" [14]. Another definition for residual stress was given by Macherauch et al. [15]. They defined "residual stresses as those stresses that act in a closed body, which is free of any external load. The mechanical forces and moments related to them must compensate each other with respect to any macroscopic cross-section and axis through the body, respectively; otherwise the body would elongate or bend, which is obviously not the case". These definitions tell us principally the same but they do not tell anything about the linear dimension, on which the residual stresses act. A definition that defines these stresses by means of different length scales for the polycrystalline aggregate, which is in this case a thin film consisting of many crystallites, had to be found. With the information of the crystalline film structure a division of the residual stresses within the material into a first-, second- and third type stresses are possible. The type I stresses, which are also called *macro stresses*, is the volume average over all crystallites and phases within a volume [15]. They are distributed homogeneously over macroscopic distances, i.e. several grains and are often developed during sample manufacturing. The type II, *micro stresses*, are homogeneous over microscopic areas

such as one grain or sub-grain. They occur because of the mismatches in thermal and mechanical properties of the individual phases or grain orientations. The third type, also called *root mean square (r.m.s.) stresses*, is a micro stress too, but inhomogeneous within sub-grains or crystallites. They occur due to the presence of lattice imperfections, and vary on the atomic scale [16].

2.2.2 Origin of residual stresses

In the paragraphs above, an introduction and classification of the residual stresses was made rather formally what is certainly useful when one would like to analyze the residual stress state in thin films by x-ray diffraction. For the material scientists and thin-film engineers who deal with the deposition process of thin films, the correlation between the residual stresses stored in the films and their origin in the process of deposition is of more interest.
Inhomogeneous plastic deformations with respect to any sample cross section or to any macroscopic sample area are the reason for the origin of long-range macro stress or phase-specific residual stress fields in polycrystalline materials. The elastic strain between individual parts of the technical compounds is another important source for macro residual stress which especially applies to thin films deposited on any kind of substrate (amorphous, single- or polycrystalline). Corresponding to their origin in the film deposition process, one can distinguish between extrinsic and intrinsic residual stresses.
The *extrinsic* residual stresses can generally be defined as the thermal stresses which occur because of the difference of the coefficients of thermal expansion between the film and the substrate. Figure 2.5 shows schematically the origin of such an extrinsic stress, where α_s and α_f are the coefficients of thermal expansion of the substrate and the film, respectively [15].
Stresses which having lattice inherent origins are termed as *intrinsic* stresses. For example, in single-crystals hetero-epitaxy as shown in Figure 2.6 (a), where a_f and a_s are the lattice parameters of the film and the substrate, respectively results in misfit induced stresses. Figure 2.6 (b) shows another origin for intrinsic film stresses, i.e. defect incorporation into the film during deposition. In detail, the formation of non-equilibrium structures, re-crystallization, grain boundary relaxation, ion bombardment or crystallite coalescence contribute to the generation of intrinsic stresses. They are of particular interest in chemical (CVD) and physical (PVD) vapor deposition of polycrystalline films [15].

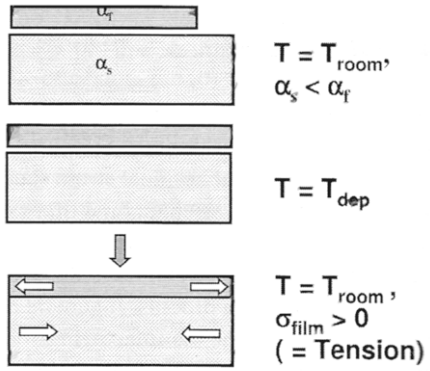

Fig. 2.5: Thermal stress due to the difference between the coefficients of thermal expansion α, of the film and the substrate; T_{dep} is the deposition temperature [15].

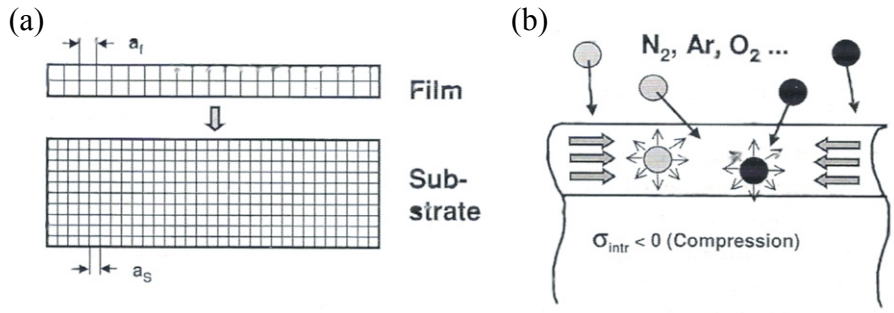

Fig. 2.6: Intrinsic residual stress: (a) the misfit-induced stress due to the mismatch between the lattice parameters of film and substrate; (b) stresses due to defect incorporation during film deposition [15].

In contrast to the thermal- or misfit-induced stresses which can be calculated by formulas, the theoretical evaluation of the residual stresses of the last group is very difficult. The reason is that their amount as well as their distribution within the growing film depends on the deposition kinetics in a complex way [15].

Several investigations by x-ray analysis in hard coatings show the relations between the coating/substrate composition, the coating process used and the development of the varying levels of residual stress. In case of CVD coatings, the residual stress occurs mainly because of the thermal mismatch upon cooling from the high deposition temperature and is, as mentioned above, essentially an extrinsic stress. Due to the thermal strain, which is introduced by the differences in the coefficients of thermal expansion between the individual layers and the substrate, the strain and stress state changes. In case of TiC, Ti(C, N), TiN and Al_2O_3 coatings on WC-Co substrates, which are of interest in this work, the residual stresses are tensile in the coating. If the fracture strain is exceeded, this tensile stresses lead to thermal cracks in the thickness direction. Under applied stress such cracks constitute preexisting flaws which can propagate into the tougher substrate [13, 16].

In summary, one can say that the effect of stresses may be minor or can be catastrophic, but on all accounts it is obviously necessary to determine the stress state within the coating.

2.2.3 Determination and modification of the stress state

Coating stresses constitute a large amount of mechanical energy which might be released by crack generation and propagation and further peeling of the layer from the substrate. The effects on the film-substrate system due to this stored mechanical energy can be detrimental [15]. Various analysis techniques [17] can be used for the determination of the residual stress in thin films. One method for coatings of thickness higher than about 0.3 mm is the *hole drilling method* where a shallow hole is drilled to a depth approximately equal to the hole-diameter. This leads to a redistribution of the stress in the material around. The strain relief can be measured by a three-element strain gage in a standardized rosette and with this the original in-plane residual stress that existed at the location of the hole can be calculated. Other methods are *deflection methods* like the *cantilever beam method* or the *disc deflection method* which are applicable to thinner coatings on thin substrates and involve measuring the bending of a coated strip or disc. Another possibility to measure the residual stress is x-ray diffraction which is a non-destructive and phase-selective analysis. There are different x-ray methods; one is the *glancing incidence method* (GID) where the stress in thin coatings or the surface of thicker coatings can be determined at depths of as small as 1 µm. In this method all peaks within the instrumentally permitted diffraction range are used and diffraction occurs at a given, near-constant depth of penetration. Another one which is of interest in this work is the *$sin^2\psi$-measuring technique* where in contrast to the first one only a single peak is used. The penetration depths of the incident beam are affected by the variation in the value of the angle which results in the presence of a stress gradient through the coating [17].

X-ray stress analysis by the $\sin^2\psi$ - technique

The x-ray stress analysis (XSA) of thin films is based on the change caused by the stress to the lattice parameters. Acting on the assumption of a biaxial stress model, all residual stresses vanish except the in-plane component. Equation 2.6 shows the reduced fundamental equation of XSA for this case where ε_ψ is the strain depending on the tilt angle ψ, ν is the Poisson's ratio, E is the elastic modulus and $\sigma_{||}$ is the in-plane stress.

$$\varepsilon_\psi = \sigma_{||} * \left[\frac{1+\nu}{E} * \sin^2\psi - \frac{2\nu}{E} \right] \tag{2.6}$$

By plotting the strain or the normalized difference of lattice versus $\sin^2\psi$, one can determine the in-plane stress $\sigma_{||}$ from the slope of the curve when the elastic modulus and the Poisson's ratio are inserted [15]. Figure 2.7 shows such a d-$\sin^2\psi$ relation, which is also named a d distribution, of an Al_2O_3 film which shows positive slope, indicating the presence of tensile residual stress. If there is a stress gradient in the coating the d-$\sin^2\psi$ relation becomes curved. Some practical difficulties because of certain inherent conditions in the specimen can affect the accuracy and even the possibility of XSA. For example, a large grain size makes the diffraction line spotty and its position not well defined. A further complication is the occurrence of texture. A crystal orientation which is non-randomly distributed may cause a Bragg reflection which is only observable for a restricted range of tilt angles.

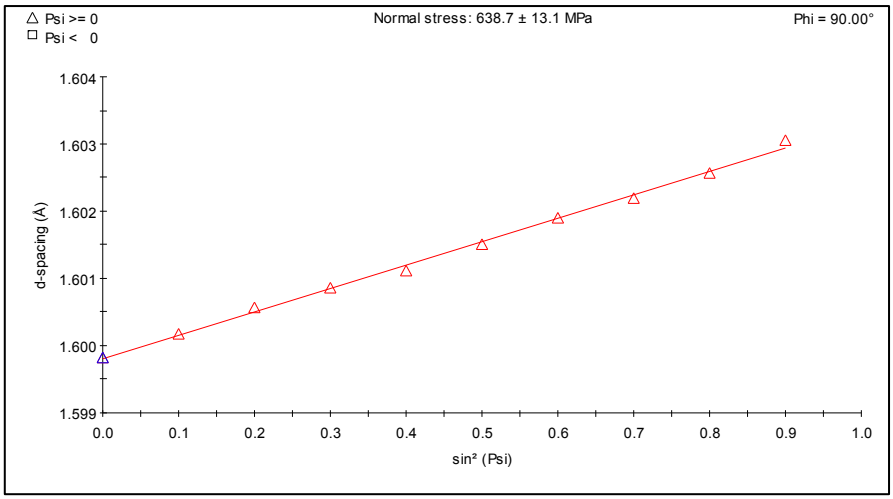

Fig. 2.7: A d distribution of an Al_2O_3 coating [18].

Thus a reliable regression of the measured strain distribution is impossible. A second effect of texture is the measured value of the elastic modulus which depends markedly on the direction of the specimen if the material is elastically very anisotropic [15, 19]. It can be seen that the x-ray residual stress analysis of coatings is a quite difficult and demanding procedure.

Modification of the stress state

As mentioned above cemented carbide cutting tools coated by CVD with TiN, TiC, Ti(C, N), Al_2O_3 or its combinations show tensile stresses. By introducing compressive stresses in post treatment processes, the residual stress conditions can be influenced and thus the wear resistance and toughness increased. Blasting (dry or wet) is such a post treatment process, where the contact stresses arise from the kinetic energy of particles, e.g. corundum, in air or liquid stream as it encounters at a surface [20]. The wear rate behavior can be adjusted by the impact angle, shot velocity, peening time and hardness rate of shot and workpiece. If the

hardness of the shot is higher compared to that of the workpiece, compressive stresses will be introduced because surface stretching occurs. To increase compressive stresses in the coating and the substrate, high impact pressures are needed which can be obtained in a dry blasting process. It is possible to tailor residual stresses, but properties like coating thickness, composition, grain size, texture and adhesion are very important points which can influence the results of the blasting process significant [20].

2.3 Nanoindentation testing and evaluation

Indentation testing is a simple method for probing the mechanical properties of materials such as elastic modulus and hardness. This technique consists essentially of intending the material of interest, where the mechanical properties are unknown, with another material whose properties are known. Such methods relate the applied load to a geometrical feature of the remaining indent which is evaluated in size by optical or other methods.
In case of thin films, the residual indents reach a size of only a few microns or even less, which makes it very difficult to obtain a direct measure using optical techniques. Another problem is that the penetration depth is limited to usually less than 10 % of the film thickness to avoid or reduce the influence from the substrate. The solution is depth-sensing or instrumented indentation. This type of indentation testing is termed “nanoindentation” because of its usual application to depths of penetration in the sub-micron range [21]. This type of test also consists of penetrating the material with an indenter, but the area of contact and hence the hardness and elastic modulus is determined indirectly using the applied load and the depth of penetration which are recorded during the test. In some circumstances, other properties like strain-hardening index, fracture toughness, yield strength and residual stress can also be obtained [22]. In indentation testing, different indenter types are in use like a spherical indenter, Vickers diamond pyramid indenter, cube corner indenter, Knoop indenter or the Berkovich indenter. For nanoindentation testing, the three-sided Berkovich indenter is the most common indenter because its tip can be made very sharp and thus the line of conjunction usually found in a four-sided Vickers indenter can be avoided [21-22]. Figure 2.8 (a) shows a cross sectional schematic of an indentation with such a pyramidal indenter under the load F. The determination of elastic modulus and hardness of a specimen material from experimental readings of indenter load and depth of penetration is the principal goal of nanoindentation testing. The essential element in this procedure is the load-displacement curve, where load and depth of penetration are recorded as load is applied from zero to some maximum and backwards. Usually such a curve, which is shown in Figure 2.8 (b), consists of a loading part, containing elastic and plastic deformation, followed by an unloading part which usually is thought to be wholly elastic. As mentioned above, the elastic unloading curve can be used with elastic equations of contact to determine the area of contact (A) at full

load (F_{max}). From this contact area the mean contact pressure and, thus, hardness (H) can be estimated by the definition in Equation 2.7 [21-23].

$$H = \frac{F_{max}}{A} \tag{2.7}$$

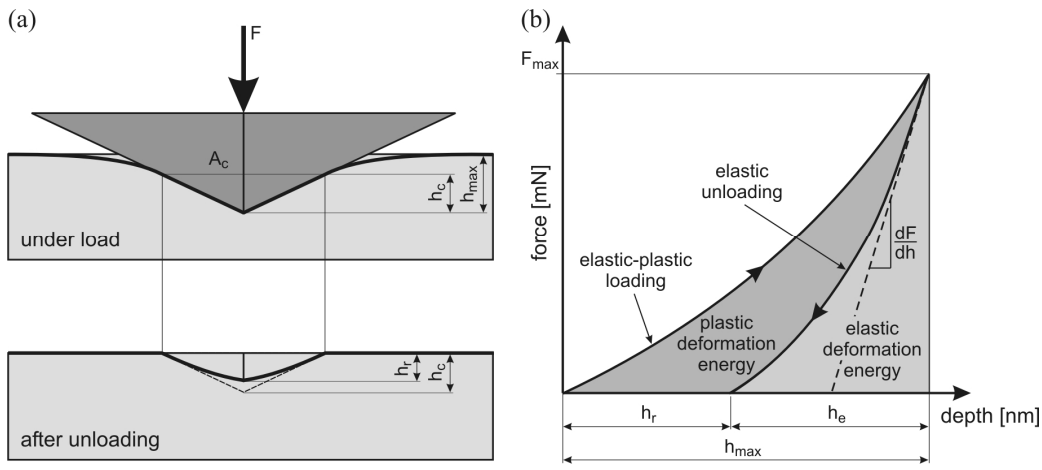

Fig. 2.8: (a) Schematic illustration of indenter (pyramidal) and specimen surface geometry at full load and full unload; h_{max} is the total depth of penetration; h_c is the depth where the indenter is in contact with the material; h_r is the depth of the residual indent after unloading; A_c is the contact area; (b) corresponding load displacement curve, h_e is the elastic displacement during unloading [24].

The elastic modulus E can also be determined by the area in combination with the slope of the unloading curve dF/dh, which is called the contact stiffness. Equation 2.8 shows the elastic modulus as a function of dF/dh and A.

$$E = \frac{1}{2} * \frac{\sqrt{\pi}}{\sqrt{A}} * \frac{dF}{dh} \tag{2.8}$$

It can be seen in Figure 2.8 (b), that the load-displacement curve during unloading is not linear, even in the initial stages. Oliver and Pharr [23] established a method to solve this problem. They found that the usually not linear unloading data are better described by a power law. This method builds on solutions by Doerner and Nix who suggested that unloading stiffness could be computed from a linear fit of the unloading curve. By extrapolating the linear portion of the curve to load zero, the extrapolated depth h_r (see Figure 2.8 (b) could be used to determine the contact area and thus the mechanical properties of the specimen [23].

In nanoindentation testing several errors can influence the instrumented data, thus it is necessary to account for various sources of error [25] before arriving at a final value for the mechanical properties of the material.

The first one is the *initial penetration depth*. Theoretically, the indenter displacement is ideally measured from the level of the specimen surface, but in practice the indenter must first make contact with the specimen surface before the measure of the displacement can be taken. Thus, to establish the onset for the test displacement measurement, it is necessary to make actual contact with the specimen surface. To get an initial contact depth as small as possible, the smallest obtainable force of the instrument is used. Nevertheless, a small corresponding penetration of the indenter beneath the undisturbed specimen free surface occurs. To avoid that all subsequent displacement measurements taken from this onset will be in error; this small initial penetration depth has to be added to all displacement measurements.

The second important error in depth-sensing indentation is the *frame compliance*. This is the contribution to the depth readings arising due to load frame deflections, instead of displacement into the material. When load applies, the reaction force is taken up by deflection of the load frame. This deflection is typically added to the depth readings. To correct this error, the product of the known instrument compliance and the force has to be subtracted from the depth reading as recorded by the instrument.

The third common and necessary correction is the *indenter area function*. It is a function, or a table of values, providing the best estimate of the area of contact, as a function of the contact depth, for the used indenter. It contains the correction factor needed to account for non-ideal indenter geometry. Usually, indenters are made with high precision and accuracy regarding the face angles, but no indenter is perfect. The ideal geometry often breaks down near the very tip, where tip rounding occurs due to the use of the indenter or just from the manufacturing process. The area function can be found by testing a material of known modulus or hardness and determine the value of A as a function of the contact depth over the load range of the instrument [21-22, 25].

Additionally to the above mentioned errors, there are various material-related effects which can cause errors in the estimation of modulus and hardness. The most significant of these material issues is that of piling-up and sinking-in. Elastic equations of contact assume the contact circle being beneath the specimen surface. Instead, in this case, the material may be pushed upwards around the edges or significantly sink-in. Other effects which can influence the measurement are indentation size effects like the homogeneity of the material, the presence of residual stresses and strain-hardening due to specimen preparation and polishing procedure, and the presence of friction between the indenter and the specimen [21].

Nanoindentation testing of thin films is the main application of depth-sensing indentation, but as mentioned above, specific care is needed in the interpretation of the results.

2.4 Modeling

The software used in this work is ELASTICA [26-27], which allows to model linear elastic contact problems on layered materials in a very fast way. So, some fundamentals concerning contact mechanics which are of importance in this work will be presented in the next sections.

2.4.1 Contact mechanics

Hertz contact pressure distribution

Hertz was the first who studied the nature of stresses arising from the contact between two elastic bodies [22]. He was particularly interested in the nature of the localized deformation and the distribution of pressure between two elastic bodies placed in mutual contact. Hertz assigned a shape of the contact surface which satisfies certain boundary conditions, namely [22]:

i. The differential equations of equilibrium for elastic bodies must be satisfied by the displacements and stresses, and at a huge distance from the contact surface the stresses must vanish.
ii. The contact between the bodies is frictionless.
iii. The normal pressure, at the surface of the bodies, is zero outside and equal and opposite inside the circle of contact.
iv. Inside the circle of contact, the distance between the surfaces is zero and higher than zero outside.
v. With respect to the area of the circle of contact, the integral of the pressure distribution within the circle of contact gives the force acting between the two bodies.

Hertz deduced that in case of a sphere, these conditions are satisfied by an ellipsoidal distribution of pressure shown in Figure 2.9.

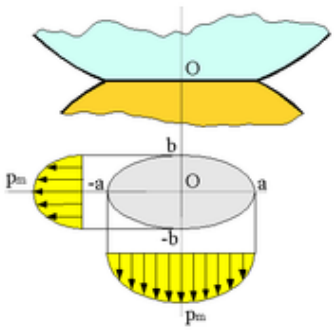

Fig. 2.9: Hertzian pressure between two curved bodies [28].

Equation 2.9 gives the distribution of normal pressure σ_z directly beneath a spherical indenter. p_m is the mean contact pressure, a the contact radius and r the distance from the axis of indentation.

$$\frac{\sigma_z}{p_m} = -\frac{3}{2}\left(1-\frac{r^2}{a^2}\right)^{1/2}, \; r \le a \tag{2.9}$$

The maximum of the pressure distribution, which is 1.5 times the mean contact pressure, was reached at the center of contact and falls to zero at the edge of the circle of contact (r = a), see Figure 2.9 [22].

Hertz contact equations

Hardness testing and modeling with ELASTICA are only two practical applications of the stresses and deflections arising from the contact between two elastic solids. In case of this work, the contact between a rigid sphere and a flat surface is of particular interest. Hertz found that for this case the radius of the circle of contact a, is related to the indenter load P, the indenter radius R, and the elastic properties of the materials which is shown in equation 2.10.

$$a^3 = \frac{3}{4}\frac{PR}{E^*} \tag{2.10}$$

E^* is the combined modulus of the indenter and the specimen given by equation 2.11:

$$\frac{1}{E^*} = \frac{\left(1-\nu^2\right)}{E} + \frac{\left(1-\nu_1^{\,2}\right)}{E_1} \tag{2.11}$$

E and ν, and E_1 and ν_1, are the elastic modulus and Poisson's ratio of the specimen and the indenter, respectively.
An equation for the mean contact pressure, p_m is given in equation 2.12, where the indenter load P is divided by the projected contact area [21-22, 25].

$$p_m = \frac{P}{\pi a^2} \text{ with re-insertion of Eq. (2.10) } p_m = \left[\frac{4}{3}\frac{E^*}{\pi}\right]\frac{a}{R} \tag{2.12}$$

For understanding the process of indentation and the nature of the contact between elastic solids, Hertz made the following assumptions to facilitate the analysis [22]:

i. The radius of the circle of contact is small compared with the radii of curvature of the contacting bodies.
ii. Compared with the radius of the circle of contact, the dimensions of each body are large. Thus, indentation stresses and strains could be considered independently of those arising from geometry, method of attachment, and boundaries of each solid.
iii. The contact between the bodies is frictionless. Only a normal pressure is transmitted between the indenter and the specimen.

The simulation in this work has been done with a spherical indenter. A spherical indenter on a homogenous half-space generates the so called Hertzian pressure profile. In practice it is also known, that if an upper layer of the half-space has different elastic properties, the resulting pressure distribution on the surface is more or less different from the Hertzian one. But despite the conditions and assumptions mentioned above, the Hertzian pressure profile could be taken as a rather good approximation for the real conditions [29].

Von Mises failure criterion

To predict the durability of layered compounds by a reliable modeling approach, knowledge of failure criteria is of paramount importance. Plastic deformation is considered to be a condition of failure of the specimen under load. It is a mechanism which is caused by stresses exceeding the yield of fracture strength. There are various failure criteria which attempt to predict the onset of plastic deformation, e.g. the Tresca criterion or the von Mises comparison stress [1, 22]. The von Mises stress is the most important stress criteria for the onset of plastic deformation and therefore for the estimation of the load carrying capacity of coated systems. It is calculated according to equation 2.13:

$$\sigma_m = \sqrt{\frac{1}{2}\left[\left(\sigma_{xx} - \sigma_{yy}\right)^2 + \left(\sigma_{zz} - \sigma_{yy}\right)^2 + \left(\sigma_{xx} - \sigma_{zz}\right)^2 + 6 * \left(\tau_{xy}^2 + \tau_{xz}^2 + \tau_{zy}^2\right)\right]} \tag{2.13}$$

σ_{ii} are the normal stresses parallel to the Cartesian coordinate axis and τ_{ij} are the related shear stresses. Thus, a complicated multiaxial stress state can be brought into connection with the uniaxial tensile or compression test. The yield stress Y corresponds to a critical value, $\sigma_{M,crit}$, of the von Mises stress, and if this value is exceeded, plastic deformation starts. The maximum von Mises stress in an indentation, with a spherical indenter on a homogenous material, will be along the z axis, i.e. along a line perpendicular to the sample surface. The shearing components τ are all zero along the z axis and σ_{xx} and σ_{yy} are equal [2, 30].

2.4.2 Software package ELASTICA

The aim of this thesis is the modeling of a layered system to calculate the critical stress state where failure starts. This can be done by Finite Element (FE) or Boundary Element (BE) methods which have the disadvantage of a long calculation time. ELASTICA is a software package for the analytical calculation of stresses in layered media under spherical indentation, which are used in this work. It has been developed at the Technical University of Chemnitz in Germany [30]. A screenshot of the software is shown in Figure 2.10. ELASTICA allows applying contact mechanics in an easy and user friendly way. It enables to calculate three-dimensional stress and deformation fields in coated systems during an elastic surface contact due to a Hertzian pressure distribution. Further, elastic force-displacement curves for different indenter types for a highly accurate film modulus determination can be calculated and compared with experimental indentation data. With this software one can get a quick estimation of the load carrying capacity of the coated systems investigated and useful conclusion on optimizing layer architectures and thicknesses can be drawn. In ELASTICA up to three layers on a substrate can be investigated [27].

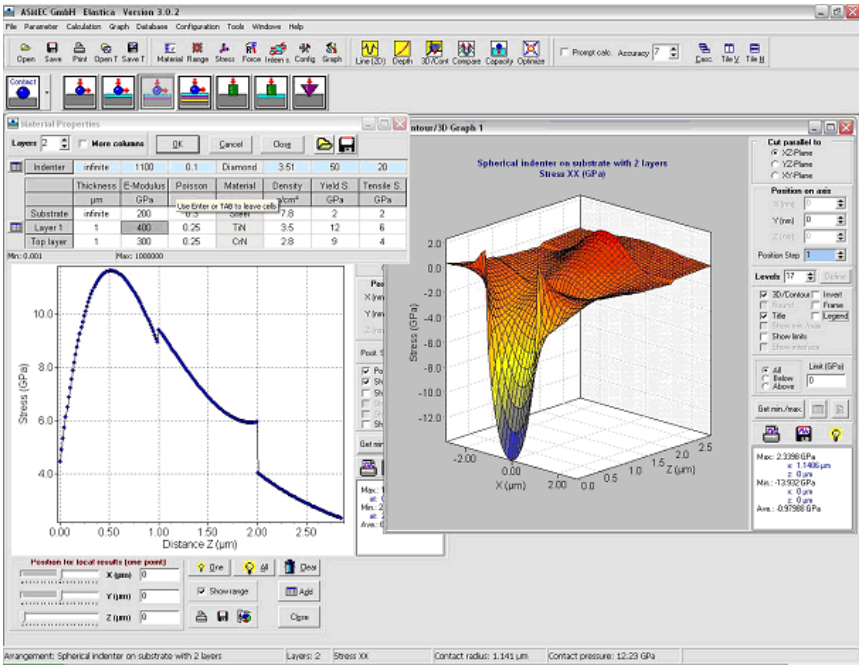

Fig. 2.10: Screenshot of the surface of the modeling software ELASTICA [26].

The main assumptions, which were made in ELASTICA [26], are that the materials are homogenous and isotropic; that the surface and interfaces are ideally flat and that there is an ideal adhesion of the coatings. Despite these idealizations, the model leads to useful results as demonstrated, for example by Chudoba et al. [2] and Eller [1].

3 Experimental and modeling details

When dealing with engineering mechanical contacts like those occurring for coated cemented carbide inserts during turning (Figure 3.1(a)), two different scales must be considered. One is the contact on microscopic scale, shown in Figure 3.1(b), where the surfaces never are perfectly smooth and thus the surface asperities can influence experimental measurements like nanoindentation [31], as used in this thesis. The second one is the macroscopic contact (Figure 3.1(c)), where a stress distribution, caused by the curvature of the component, occurs. This is the case by modeling with ELASTICA where an ideal flat surface of the counter-body is assumed.

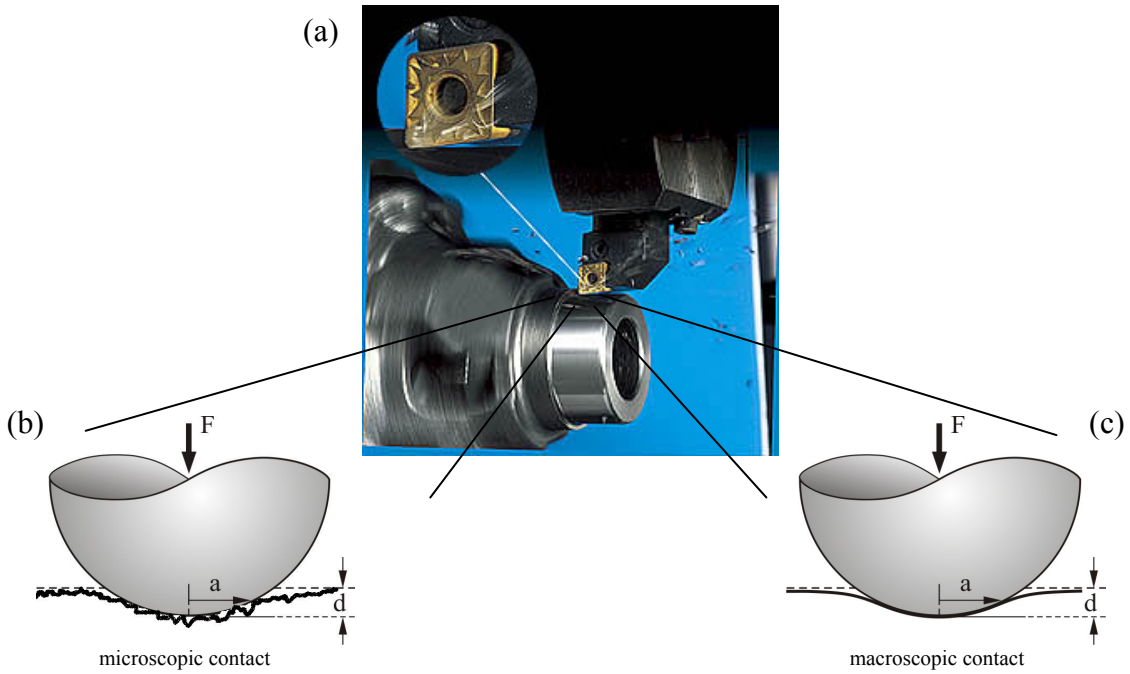

Fig. 3.1: (a) Cutting insert during turning process. Contact between a sphere and an elastic half-space at load F for (b) microscopic and (c) macroscopic scale; a is the contact radius and d the indentation depth [32-33].

3.1 Nanoindentation measurements

Nanoindentation experiments to obtain values of the elastic modulus of the coated inserts were performed using an ultra micro indentation system (UMIS) and a CSM Nano Indentation tester. The modulus measurements were done with a Berkovich indenter. The maximum load was 30 mN and twenty indents were made to secure statistical representative

values. Load and depth were recorded simultaneously and hardness and elastic modulus were analyzed, in case of UMIS by the IBIS software and by sinus mode analysis in case of the CSM tester. In Table 3.1 the measured values as well as literature values are presented.

Tab. 3.1: Obtained values of the elastic modulus for the two different nanoindentation instruments, as well as literature values.

Layer	Elastic modulus measurements [GPa]			Citation
	UMIS	CSM	Literature	
WC-Co	/	/	540	CERATIZIT [33]
TiN	/	524	418 - 556	Kutschej et al. [34]
TiCN	420	538	400	Kral et al. [35]
TiCO	218	471	/	/
α-Al_2O_3	396	400	424.6	Ruppi et al. [11]
κ-Al_2O_3	295	323	344.3	Ruppi et al. [11]

3.2 Determination of cutting force and contact area

To do modeling at real conditions of cutting, parameters like the cutting force, contact area and thus pressure are needed. Quinto [13] found that during continuous turning pressures between about 1900 and 4900 N/mm^2 are exerted on the tool tip. Using cutting data from CERATIZIT Austria [36], the assumed "real" contact area and the pressure during a turning test could be estimated. The contact area was calculated by multiplication of the feed rate with the cutting depth and Equation 3.1 shows the formula to calculate the pressure P.

$$P = \frac{F}{A} = \frac{cutting\ \ force}{contact\ area} \tag{3.1}$$

The information like feed rate, cutting depth and cutting force as well as the determined contact area and pressure are summarized in Table 3.2 for different cutting conditions.

Tab. 3.2: Data from turning tests on a CK60 (V960) steel for the determination of the theoretical contact area and pressure [36].

feed rate [mm]	cutting depth [mm]	contact area [mm^2]	cutting force [N]	pressure [N/mm^2]
0.52	4	2.08	5197	2498.56
0.4	4	1.6	4346	2716.25
0.2	4	0.8	2380	2975.00
0.4	2	0.8	2341	2926.25
0.2	2	0.4	1291	3227.50
			average value: 3111	

From Table 3.2, an average cutting force of 3111 N and a maximum contact area of 2.08 mm^2 were obtained. By using this "real force" and varying the indenter radius in the ELASTICA modeling software, a radius of about $90*10^3$ µm was found which leads to a contact radius of 824 µm. Insertion of this radius in the formula for a circular area led to a contact area of about 2.13 mm^2 which equates nearly the determined value above. Thus, for modeling "real" conditions in ELASTICA, a force of 3111 N and an indenter radius of about $90*10^3$ µm were used.

3.3 XRD analysis

The x-ray diffraction (XRD) stress analyses were carried out at CERATIZIT Luxembourg on a Panalytical X'Pert Pro diffractometer using copper K_α-radiation and a flat graphite monochromator. The residual stresses were determined with the $\sin^2\psi$-technique mentioned in chapter 2.2.3. As described in chapter 2.2, the residual stresses of CVD hard coatings on cemented carbide are often tensile. In case of α-Al_2O_3, Hochauer et al. found these tensile stresses to be about 570 MPa [37]. To influence the residual stress status in the coating and avoid or decrease tensile stresses, post-treatment processes like blasting, where compressive stresses are introduced, can be applied (see chapter 2.2.3). Holzschuh et al. [20] showed that by blasting compressive stresses up to -7.6 GPa in Al_2O_3 coatings can be obtained. To elucidate how the compressive stress influences the stress distribution in the coating, modeling was done with compressive stresses in the range of 0 – 10 GPa.

3.4 Modeling with ELASTICA

For modeling, version 3.0.7 of the ELASTICA software was used. The obtained elastic values and intrinsic stresses of the layers were inserted into the software and line graphs with the stress-depth profile were plotted. The forces used in ELASTICA are in the range of 30 mN to 700 mN and in the real case 3111 N. The radius of the spherical indenter varies from 10 µm up to 1000 µm and is about $90*10^3$ µm in the real case. Investigations were made for the uncoated substrate, hypothetical one-layer systems and a three-layer system. In case of the hypothetical and three-layer systems, investigations with and without compressive stresses were made.

4 Results and discussion

The layer system of interest in this work is shown in Figure 4.1(a). It is a system of five layers where each layer has a different thickness and properties which are summarized in Table 4.1. First attempts with ELASTICA, modeling the three-layered TiN/MT-TiCN/HT-TiCN system on the WC-Co-substrate, have shown that the TiN-layer has no significant influence on the system related to the von Mises stress-depth profile. The reasons for this are that the layer has only a thickness of about 0.4 µm and the elastic modulus is similar to the elastic modulus of the substrate and the MT-TiCN layer (see Table 4.1). Furthermore, these first attempts showed that the HT-TiCN-layer, which is also very thin, has also no detectable influence. These first modeling activities lead to a "reduced" layer system of only three layers shown in Figure 4.1(b), where the TiN-layer has been removed and only one TiCN-layer exists.

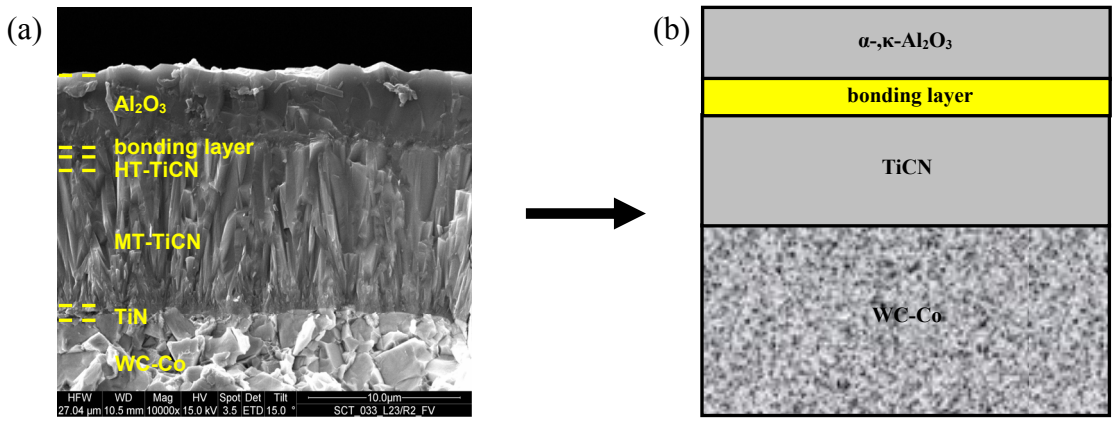

Fig. 4.1: (a) SEM cross section micrograph of the investigated layer system; (b) Schematic of the reduced layer system.

Tab. 4.1: The properties of the cemented carbide substrate and the five different layers of the investigated system.

Layer	Layer thickness [µm]	Elastic modulus [GPa]
WC-Co	infinite	540
TiN	0.4	524
MT-TiCN	9	538
HT-TiCN	0.9	444
TiCO (bonding layer)	0.4	471
Al_2O_3	5	280 - 450

4.1 Input data for modeling

The input data of the different layers for the modeling software are shown in Table 4.2. The Table is divided in two sections, the *Hypothetical* and *Reduced* layer system. The hypothetical layer system covers one-layer coatings with two different elastic moduli and two different layer thicknesses, to illuminate the influence of these two parameters. Because of the complexity of nanoindentation measurements, which can be seen in the different values obtained for the elastic modulus (Table 3.1), two different values were chosen, where the measured values lie in between. The reduced layer systems are three layer arrangements with two different Al_2O_3 layers on top. Here the used values of the elastic modulus are those measured by nanoindentation.

Tab. 4.2: Input data for modeling with ELASTICA.

		Elastic modulus		Poisson's ratio	Layer thickness [μm]
		E_{min} [GPa]	E_{max} [GPa]		
Hypothetical layer system	Substrate WC-Co	540		0,22	infinite
	TiN	400	550	0.25	1 + 2
	TiCN	450	550	0.162	1 + 2
	α-Al_2O_3	350	450	0.231	1 + 2
	κ-Al_2O_3	280	450	0.22	1 + 2
Reduced layer system	Substrate WC-Co	540		0.22	infinite
	TiCN	538		0.162	10
	TiCO	471		0.24	0.4
	α-Al_2O_3	400		0.231	5
	κ-Al_2O_3	323		0.22	5

Figure 4.2 shows an example of a two-dimensional ELASTICA plot where the ordinate (y-axis) outlines the von Mises stress and the abscissa (x-axis) outlines the depth. An explanation of the different values (σ_{max}, position σ_{max}, σ_{step}, $|\Delta\ \sigma_{step}|$) obtained from the plots for further evaluation is also given. σ_{max} is the maximum von Mises stress; Position σ_{max} is the depth where the maximum was found; σ_{step} is the von Mises stress at the onset of the step; and $|\Delta\ \sigma_{step}|$ is the height of the step.

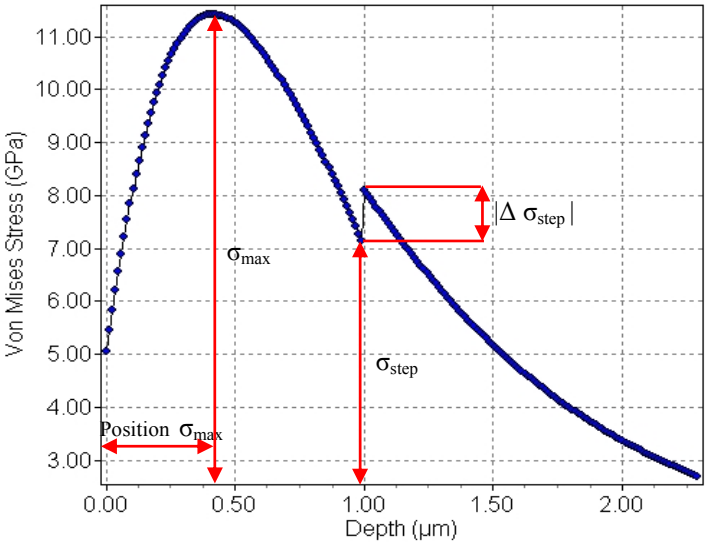

Fig. 4.2: Example of an ELASTICA plot with explanation of the different parameters taken for further evaluation.

4.2 Substrate WC-Co

First of all the uncoated WC-Co substrate was investigated. Figure 4.3 shows the ELASTICA plot with the different curves which were obtained by varying the force from 30 mN up to 700 mN. In all cases the indenter radius was 10 µm.

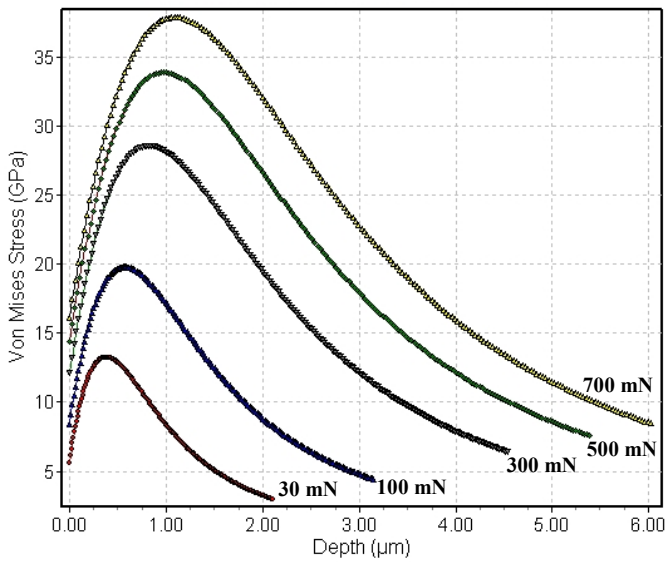

Fig. 4.3: Von Mises stress-depth profiles obtained for the uncoated WC-Co substrate at different forces and an indenter radius of 10 µm.

The curves show that the maximum von Mises stress is in the near surface region and the stress decreases with increasing depth. For example, at a force of 30 mN the maximum von Mises stress of about 12.5 GPa occurs in a depth of about 0.4 µm below the surface. With increasing force, the von Mises stress increase and the maximum moves deeper into the substrate.

In Figure 4.4 the maximum von Mises stress (σ_{max}) and the position of σ_{max} obtained from Figure 4.3 are plotted against the force at three different indenter radii.

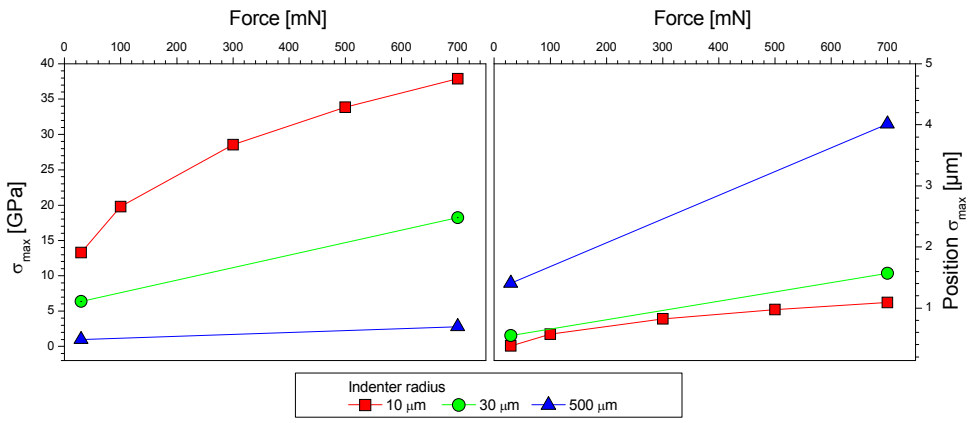

Fig. 4.4: σ_{max} and Position σ_{max} obtained for the uncoated WC-Co substrate at different forces and indenter radii.

As mentioned above, by increasing the force an increase of the maximum stress can be observed. Varying the indenter radius shows that the larger the indenter radius is, the smaller is the maximum von Mises stress. This can be explained by the acting Hertzian pressure (contact pressure per unit area) [22]. The higher the indenter radius, the smaller is the contact pressure per unit area. The position of the maximum stress moves deeper into the substrate with increasing force and indenter radius.

The results of the investigation under real conditions (real force) can be seen in Figure 4.5. The maximum von Mises stress and the position of the maximum are plotted against three different indenter radii. The force was in all cases the same (3111 N).

The investigations at real conditions show similar results as the investigations with the smaller indenter radii and forces. By increasing the indenter radius, the maximum stress decreases and its position increases.

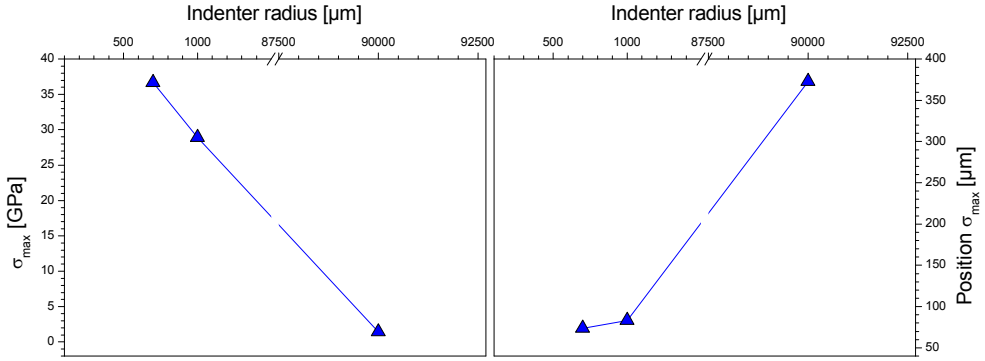

Fig. 4.5: σ_{max} and Position σ_{max} obtained for the uncoated WC-Co substrate at a force of 3111 N ("real force") and different indenter radii (700, 1000 and $90*10^3$ µm).

4.3 Hypothetical layer system

The hypothetical systems are one-layer coatings comprising of the substrate and one particular layer (TiN, TiCN, Al_2O_3). First, to present the influence of the different layer properties, i.e. elastic modulus and layer thickness, Figure 4.6 shows the hypothetical layer system of TiN with two different elastic moduli and two different layer thicknesses. The first two plots (Figure 4.6 (a) and (b)) show the influence of elastic modulus and layer thickness at a small force of 30 mN and small indenter radius of 10 µm and the last two (Figure 4.6 (c) and (d)) the influence at a higher force of 700 mN and an indenter radius of 500 µm.

Influence of the elastic modulus

The higher the elastic modulus is, the higher is the stiffness of the material. When modeling a 1 µm thick TiN-layer with two different elastic moduli (400 and 550 GPa) it can be seen that the higher elastic modulus leads to a higher von Mises stress (Figure 4.6 (a)). The maximum stress is in both curves in a depth of about 0.35 µm below the surface which is within the TiN-layer. Another difference in addition to the different maximum von Mises stress is the height of the step at the interface between the layer and the substrate (at 1 µm depth). The step in the curve with 400 GPa elastic modulus is about three times higher than that of the curve with 550 GPa. The reason for this is the huge difference of the elastic moduli of the TiN-layer and the substrate of 140 GPa. The substrate is stiffer and this leads consequently to a higher von Mises stress in the substrate and thus to the large step shown in Figure 4.6 (a). Since such steps have to be accommodated by shear stresses at the interface, they are assumed to indicate possible risks of interfacial failure [38].

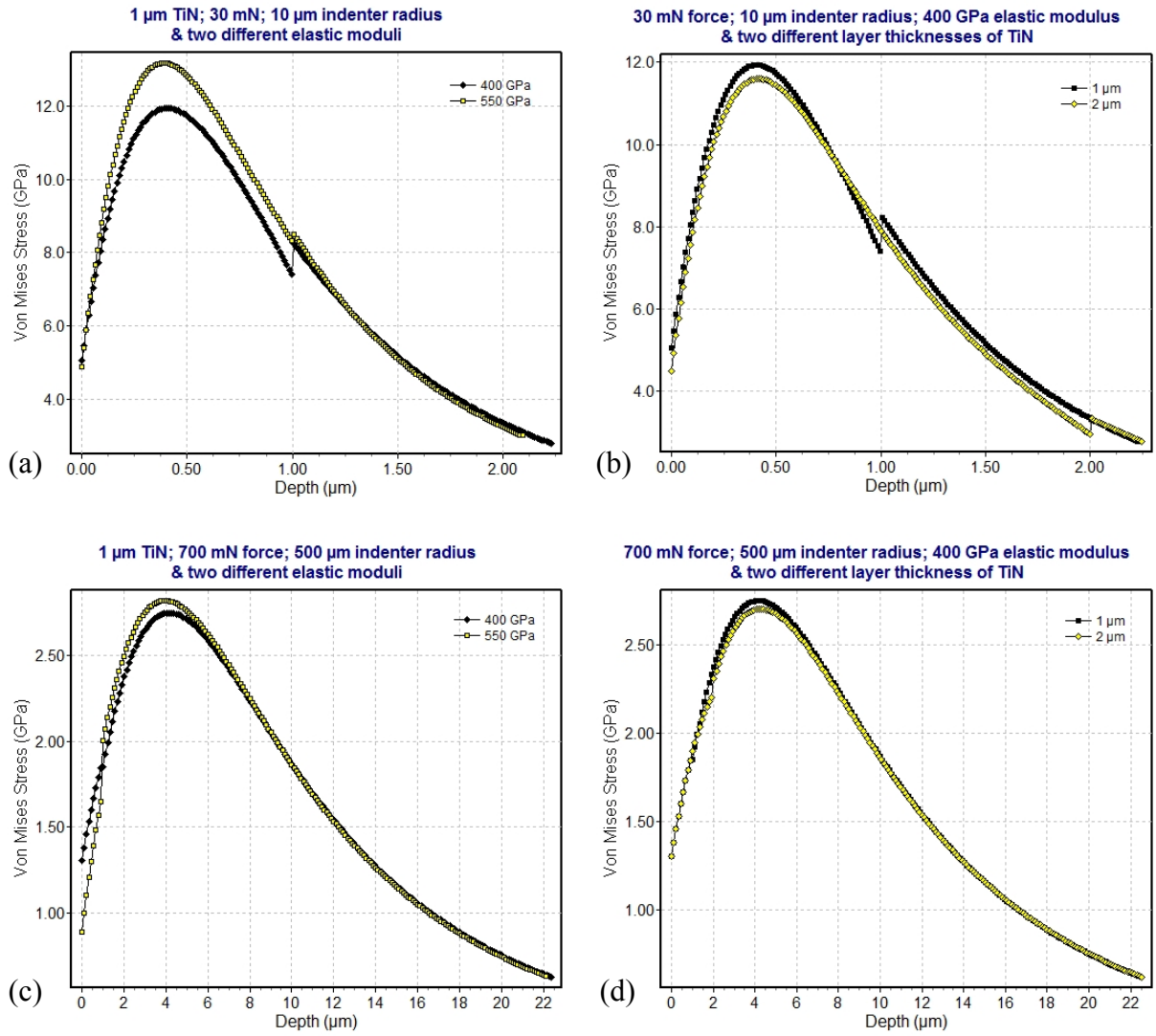

Fig. 4.6: Influence of the elastic modulus and layer thickness on the von Mises stress-depth profile of a TiN layer on WC-Co substrate at two different forces and indenter radii. The different properties (force, indenter radius, layer thickness and elastic modulus) are summarized in the header of the plots (a), (b), (c) and (d).

Figure 4.6 (c) shows the results for the modeling with higher force (700 mN) and indenter radius (500 µm). The maximum von Mises stress is much smaller than in the first case because of the smaller contact pressure per unit area [22]. The curve with the higher elastic modulus also has a higher maximum von Mises stress compared to the smaller modulus, but the difference is not as pronounced as between the curves in Figure 4.6 (a). The maximum stress is in a depth of about 4 µm which is 3 µm deep within the substrate, which is due to the higher force and indenter radius. The steps seen at the interface in Figure 4.6 (a) are in case of the higher force and indenter radius only visible as minor buckles.

Influence of the layer thickness

The smaller the layer thickness is, the higher is the influence of the under-layer, in this case the substrate. In Figure 4.6 (b) the curves obtained for the two different layer thicknesses are shown for the case of small force and indenter radius. With exception of the position of the steps, the curves are very similar. According to the different layer thickness the steps can be found. The position of the step has a significant effect on the height of the step which is in case of the thinner layer larger as can be seen in Figure 4.6 (b). The thinner layer also shows a higher maximum von Mises stress due to the influence of the substrate. The elastic modulus of the substrate is higher and due to the small layer thickness the system seems to be stiffer. In both cases the stress maximum is within the TiN-layer.
Figure 4.6 (d) shows the curves at higher force and indenter radius. They show very small deviations like the higher von Mises stress in case of the thinner layer which were explained above. On the interface between the layer and the substrate only buckles can be observed.

4.3.1 Substrate with TiN

The first hypothetical layer system investigated in detail is the system WC-Co substrate with a TiN layer. Two different force-indenter radius combinations (30 mN force/10 µm indenter radius and 700 mN force/500 µm indenter radius) were chosen. The investigations were made with two different elastic moduli of TiN (400 and 550 GPa) and layer thicknesses (1 and 2 µm). The ELASTICA plots of this system can be seen in Figure 4.6 and the results obtained from these plots are summarized in Figure 4.7, where the different parameters (σ_{max}, position σ_{max}, σ_{step}, $|\Delta\ \sigma_{step}|$) were plotted against the elastic modulus.
Figure 4.7 (a) shows the maximum von Mises stress (σ_{max}) of the eight different force/indenter radius/layer thickness/elastic modulus combinations. It can be seen, as already mentioned earlier, that a higher elastic modulus (i.e. a stiffer material) results in a higher maximum von Mises stress. The higher the force and indenter radius is, the smaller is the maximum because of the smaller contact pressure per unit area. In case of the higher elastic modulus, there is nearly no influence of the layer thickness because the elastic modulus of the layer is very similar to that of the substrate. In case of the elastic modulus of 400 GPa, the difference to the elastic modulus of the substrate is huge and thus the influence of the substrate is higher. The thinner the layer, the more pronounced is the influence and thus the maximum von Mises stress. In case of the higher force and indenter radius at the higher elastic modulus, the opposite is the case. The elastic modulus of the layer is higher than of the substrate and thus the layer is stiffer. The thicker the stiffer layer is the higher is the von Mises stress. Furthermore there is no influence of the substrate.

In Figure 4.7 (b) the position of the maximum is plotted against the elastic modulus. The higher the force and the indenter radius is, the deeper in the coating/substrate system the maximum stress can be found. At high force and indenter radius, the maximum von Mises stress is within the substrate. There is also a difference in the position of the maximum stress for the two elastic moduli. The higher the elastic modulus, the stiffer is the material and the position of the maximum is in a lower depth than in case of a smaller elastic modulus. In case of the higher force and indenter radius, a difference between the two different layer thicknesses can be observed. At the elastic modulus of 400 GPa, the thicker layer has the maximum stress deeper in the substrate than the thinner layer. At 550 GPa the opposite is the case. The layer is stiffer than the substrate and the thicker the layer is the lower is the depth of the position of the maximum stress.

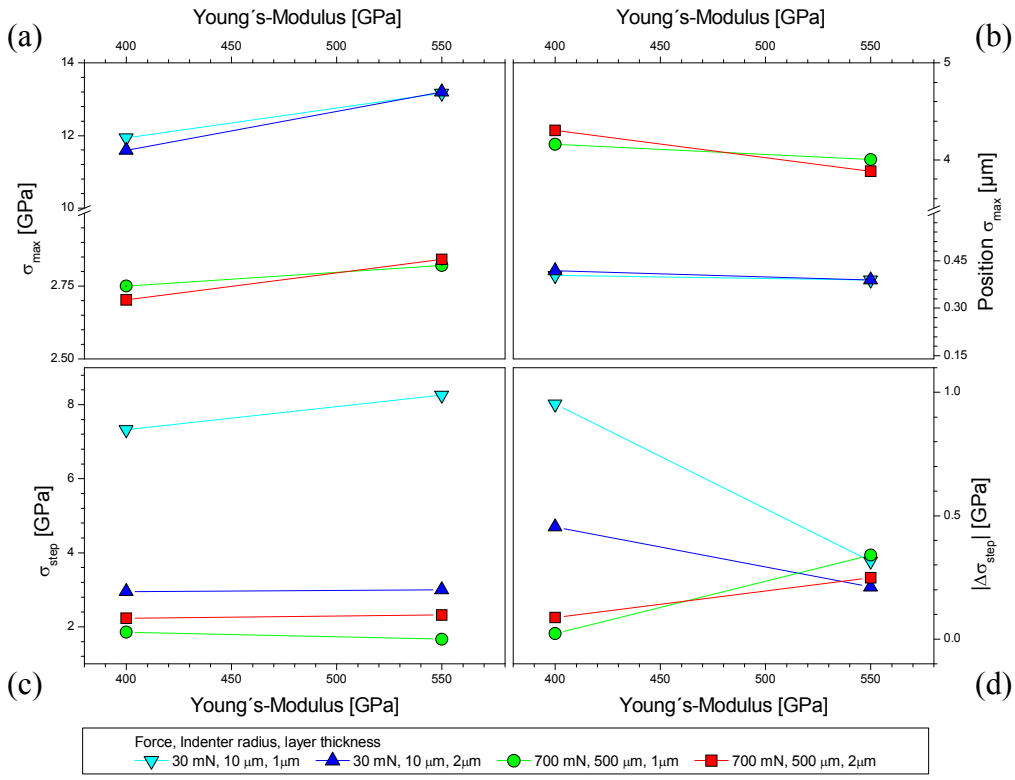

Fig. 4.7: Different parameters, σ_{max} (a), position σ_{max} (b), σ_{step} (c), $|\Delta\ \sigma_{step}|$ (d), obtained for the system WC-Co substrate with TiN layer.

Figure 4.7 (c) shows the von Mises stress at the onset of the step. The steps are located at the interface between the layer and the substrate, i.e. at the layer thickness (1 and 2 µm). At small forces and indenter radius, the maximum von Mises stress is located inside the layer, at about 0.4 µm depth and decreases afterwards. With a depth higher than position σ_{max}, the von Mises stress decreases and so the stress at the onset of the step in case of the 2 µm thick layer is smaller than for the 1 µm thick layer. For the high force and indenter radius, the opposite is

the case. The maximum von Mises stress is located within the substrate at about 4 µm from the surface, i.e. with increasing depth the stress increases further up to the maximum. Thus, it can be seen in Figure 4.7 (c) that the stress at the onset of the step is higher in case of the thicker layer. As mentioned before a higher elastic modulus leads to a higher von Mises stress and also to a higher stress at the onset of the steps. Only in the case of 700 mN force, 500 µm indenter radius and 1 µm layer thickness the stress at the onset of the step decreases slightly with increasing elastic modulus.
The height of the step, $|\Delta \sigma_{step}|$ can be seen in Figure 4.7 (d). The higher the step is, the larger is the risk of interfacial failure because of shear stresses. By adding the height of the step to the onset of the step (σ_{step}, Figure 4.7 (c)), the maximum von Mises stress of the layer or the substrate can be obtained. For example in Figure 4.6 (a), in case of the elastic modulus of 400 GPa (black curve), the maximum von Mises stress (σ_{max}) is about 12 GPa and can be observed within the TiN layer. At the interface where the step is, the maximum von Mises stress of the substrate is about 8.3 GPa. That means the yield strength, which indicates the onset of plastic deformation, of the TiN layer should be above 12 GPa and the yield strength of the substrate above 8.3 GPa. If this is the case, the substrate is protected by the thin film and will not be damaged [1].

4.3.2 Substrate with TiCN

In the second investigated hypothetical layer system, a TiCN layer instead of the TiN layer was used. In Figure 4.8 a summary of the different parameters plotted against the elastic modulus can be seen. The two different force-indenter radius combinations are the same as before (30 mN/10 µm and 700 mN/500 µm) and the two elastic moduli for the layer are 450 and 550 GPa. The results obtained for this layer system are very similar to the first one with the TiN layer instead of TiCN. In Figure 4.8 (a) the difference in the maximum von Mises stress because of the different force and indenter radius can be seen. The higher force and indenter radius leads to a smaller maximum, which can be found within the substrate (see Figure 4.8 (b)). Due to the higher contact pressure per unit area at small force and indenter radius, the higher maximum can be explained. The position of the maximum is in this case wihtin the TiCN layer (Figure 4.8 (b)). The higher the force and indenter radius is, the deeper in the layer/substrate system is the maximum von Mises stress. The decrease of the position of the maximum from the smaller elastic modulus to the higher one is because of the increasing stiffness. The von Mises stress at the onset of the step in Figure 4.8 (c) is also very similar to the first system. It depends on the location of the maximum if it is within the layer or within the substrate. At small force and indenter radius, the maximum is within the layer and the von Mises stress decreases with further increasing depth. At the higher force and indenter radius, the stress increases further within the substrate up to the maximum. The combination 700 mN

force, 500 µm indenter radius and 1 µm layer thickness also show a slight decrease of the stress at the onset of the step with increasing elastic modulus, comparable to TiN (see Figure 4.8 and 4.7 (c)).

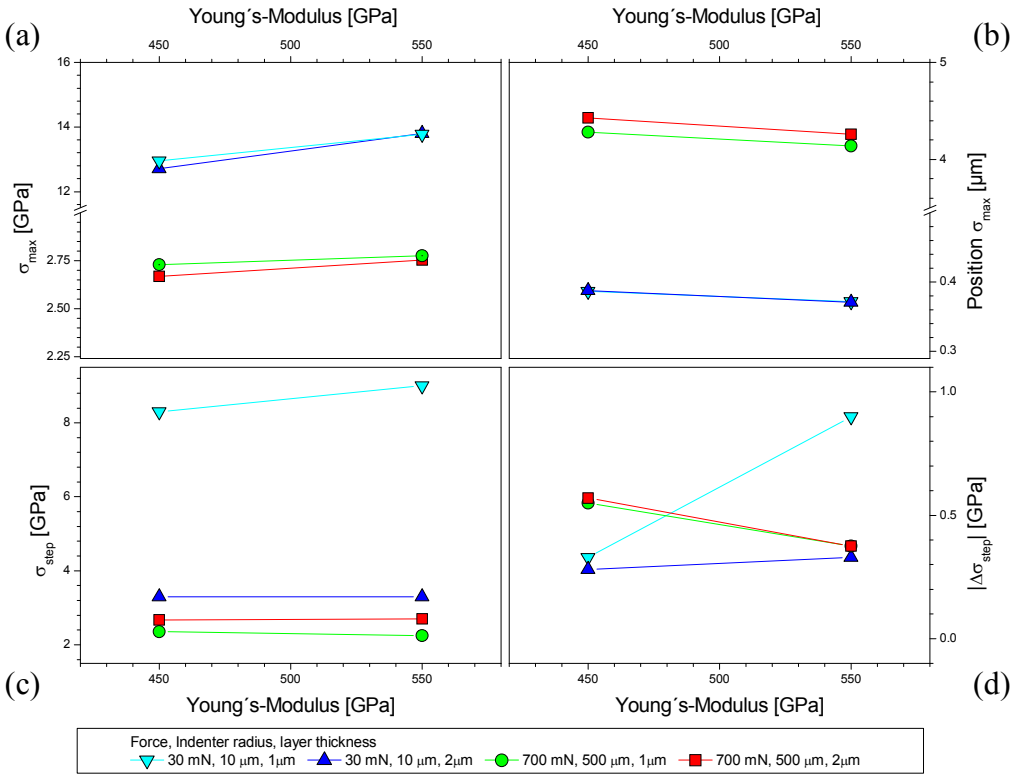

Fig. 4.8: Different parameters, σ_{max} (a), position σ_{max} (b), σ_{step} (c), $|\Delta\ \sigma_{step}|$ (d), obtained for the system WC-Co substrate with TiCN layer.

One remarkable difference between the layer systems with TiN and TiCN can be seen in Figure 4.8 (d). The height of the step increases with increasing elastic modulus in case of the small force and indenter radius. At high force and indenter radius, the height of the step decreases with increasing elastic modulus. That is exactly the opposite of the layer system with the TiN layer.

4.3.3 Substrate with κ-Al_2O_3

The next hypothetical system investigated is the system WC-Co substrate with κ-Al_2O_3. The variation in force and indenter radius is the same as before. The elastic moduli used are 280 and 450 GPa. Figure 4.9 shows the different parameters taken from the ELASTICA curves plotted against the elastic modulus. This layer system shows the same behavior regarding the maximum von Mises stress, the position of the maximum and the von Mises stress at the

onset of the step as the two systems before. The values of the maximum von Mises stress in Figure 4.9 (a) are slightly smaller than in the other cases because of the lower elastic modulus. Apart from that, the behavior is as expected; higher force and indenter radius results in a smaller maximum von Mises stress; the higher the elastic modulus is, the stiffer is the material and the higher is the maximum; and the thinner the layer is, the more pronounced is the influence of the substrate.

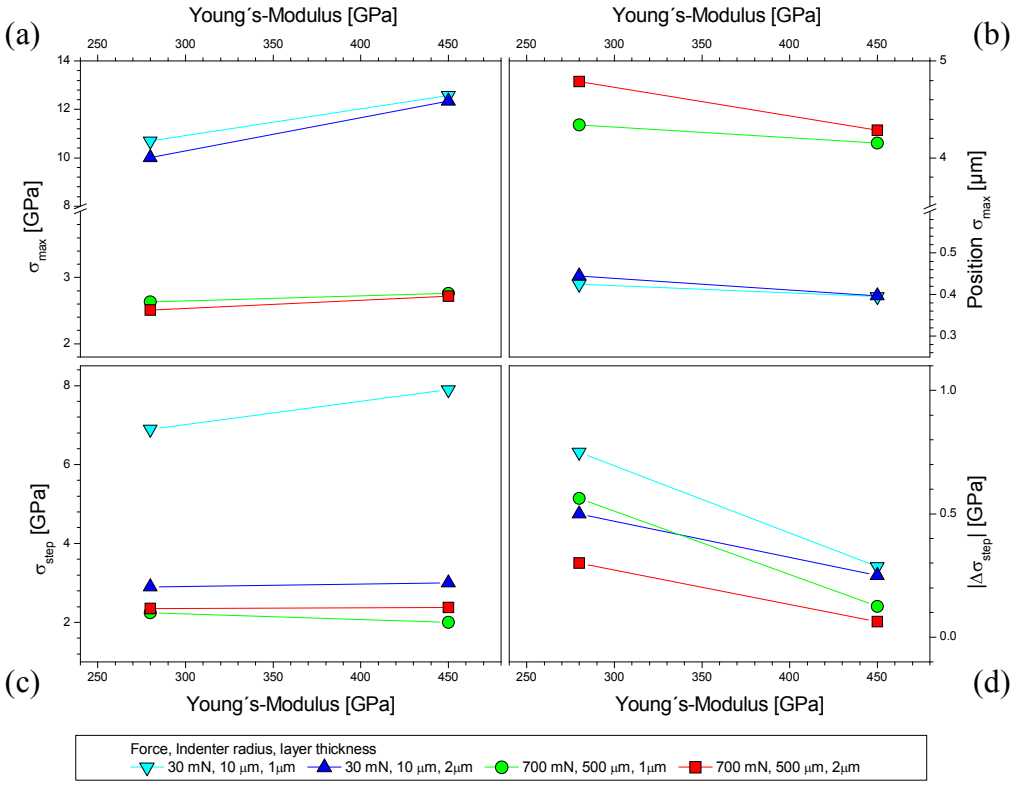

Fig. 4.9: Different parameters, σ_{max} (a), position σ_{max} (b), σ_{step} (c), $|\Delta\ \sigma_{step}|$ (d), obtained for the system WC-Co substrate with κ-Al_2O_3 layer.

Because of the smaller elastic modulus, the stiffness of the layer is lower and the maximum von Mises stress can be found at higher depth. That is in case of the higher force and indenter radius deeper within the substrate and in case of the smaller force and indenter radius deeper within the layer (Figure 4.9 (b)). The smaller elastic modulus than in the other two systems results in smaller values for the maximum von Mises stress and thus in a smaller stress at the onset of the step, as can be seen in Figure 4.9 (c). The order of the four different combinations is the same as before because of the location of the maximum von Mises stress: If the maximum is on the left side of the interface (i.e., within the layer) the von Mises stress at the onset of the step decreases with increasing depth (layer thickness). If the maximum is on the right side of the interface (i.e., within the substrate) the stress at the onset of the step increases with increasing depth. Like in the two systems before, the 1 µm thick coating at high force

and indenter radius is an exception because it is the only one where the stress at the onset of the step decreases with increasing elastic modulus (Figure 4.9 (c)). The hugest difference is like in the case of the TiCN layer in the height of the step, see Figure 4.9 (d). All four combinations concerning the force, indenter radius and layer thickness, show the same behavior. At the higher elastic modulus, a smaller height of the step can be observed.

4.3.4 Substrate with α-Al_2O_3

α-Al_2O_3 on WC-Co substrate is the fourth investigated hypothetical system. The elastic moduli in this layer system are 350 and 450 GPa. Force, indenter radius and layer thickness are the same as before. Figure 4.10 shows the obtained results of this system. It can be seen, that apart from small deviations because of the different elastic moduli, the results are very similar to the last layer system.

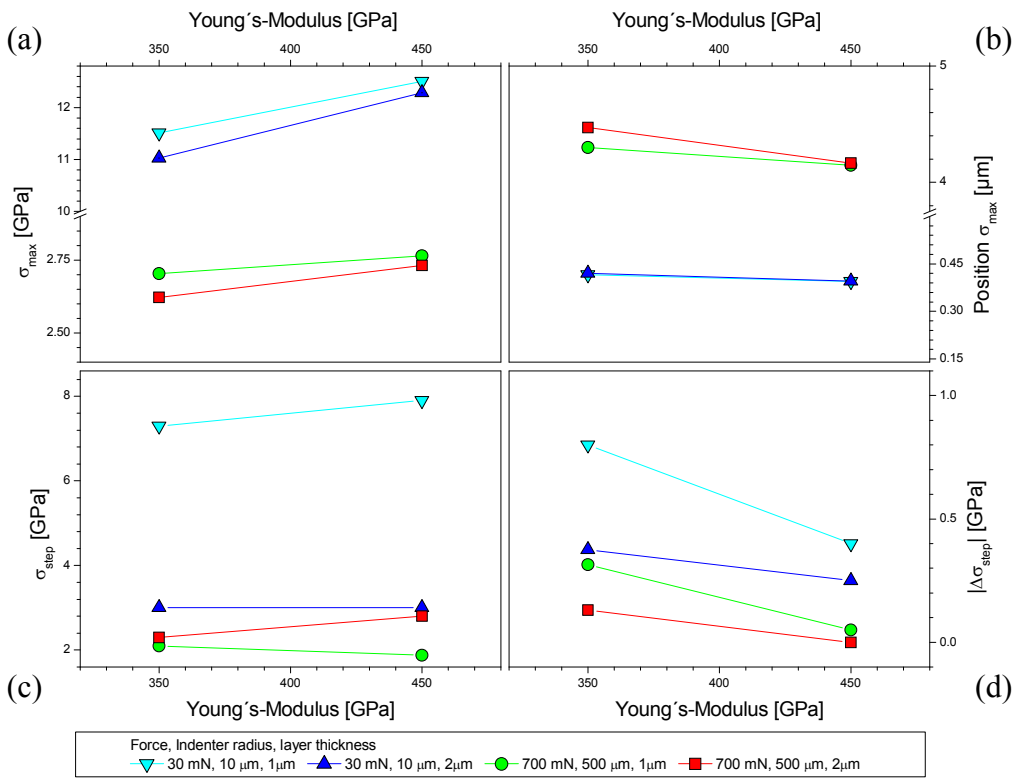

Fig. 4.10: Different parameters, σ_{max} (a), position σ_{max} (b), σ_{step} (c), $|\Delta\ \sigma_{step}|$ (d), obtained for the system WC-Co substrate with α-Al_2O_3 layer.

The influence of the force and indenter radius and also the elastic modulus regarding to the maximum von Mises stress can be seen in Figure 4.10 (a). The values of the maximum von Mises stress of the α-Al_2O_3 coating are very similar to those of the κ-Al_2O_3 coating. The

deviations between Figure 4.10 (a) and Figure 4.9 (a) are only due to the different scale of the y-axis and in case of the smaller elastic modulus because of the difference between them. The difference concerning the position of the maximum is also because of the different elastic moduli of α- and κ-Al_2O_3 in case of the smaller modulus (Figure 4.10 (b)). The explanations for the order regarding to the von Mises stress at the onset of the step which can be seen in Figure 4.10 (c) is the same as before and also the decreasing stress with increasing elastic modulus of the thinner coating at high force and indenter radius. The results for the height of the step in Figure 4.10 (d) show a huge similarity to those of the κ-Al_2O_3 layer (Figure 4.9 (d)). The small deviations are again because of the different elastic moduli.

4.3.5 Substrate with internally stressed α-Al_2O_3 layer

It is known and mentioned earlier in this work, that cemented carbide cutting tools coated by CVD with TiN, TiC, TiCN, Al_2O_3 or their combinations show tensile stresses [13, 16]. Also mentioned in chapter 2.2.3 is that the residual stress conditions can be influenced by introducing compressive stresses in post treatment processes and, thus, an increase in wear resistance and toughness can be achieved. Compressive stresses up to –7.6 GPa can be obtained in Al_2O_3 coatings by blasting [20]. To elucidate the influence of compressive stress on the stress distribution in the coating, ELASTICA modeling of the next hypothetical layer system, an α-Al_2O_3 coating on WC-Co substrate, was done with compressive stresses in the range of 0 – 10 GPa. The α-Al_2O_3 coating is assumed to be 2 µm thick and the elastic modulus used is 350 GPa. Modeling was done first with a small force of 30 mN and small indenter radius of 10 µm and afterwards at real conditions, i.e. 3111 N force and $90*10^3$ µm indenter radius.

Small force and indenter radius

First investigations of the effect of compressive stress were made using a force of 30 mN and an indenter radius of 10 µm. The elastic modulus of the α-Al_2O_3 layer is assumed as 350 GPa and the thickness of the coating is 2 µm. Figure 4.11 shows the six ELASTICA plots, obtained for different compressive stress levels (from 0 up to 10 GPa).

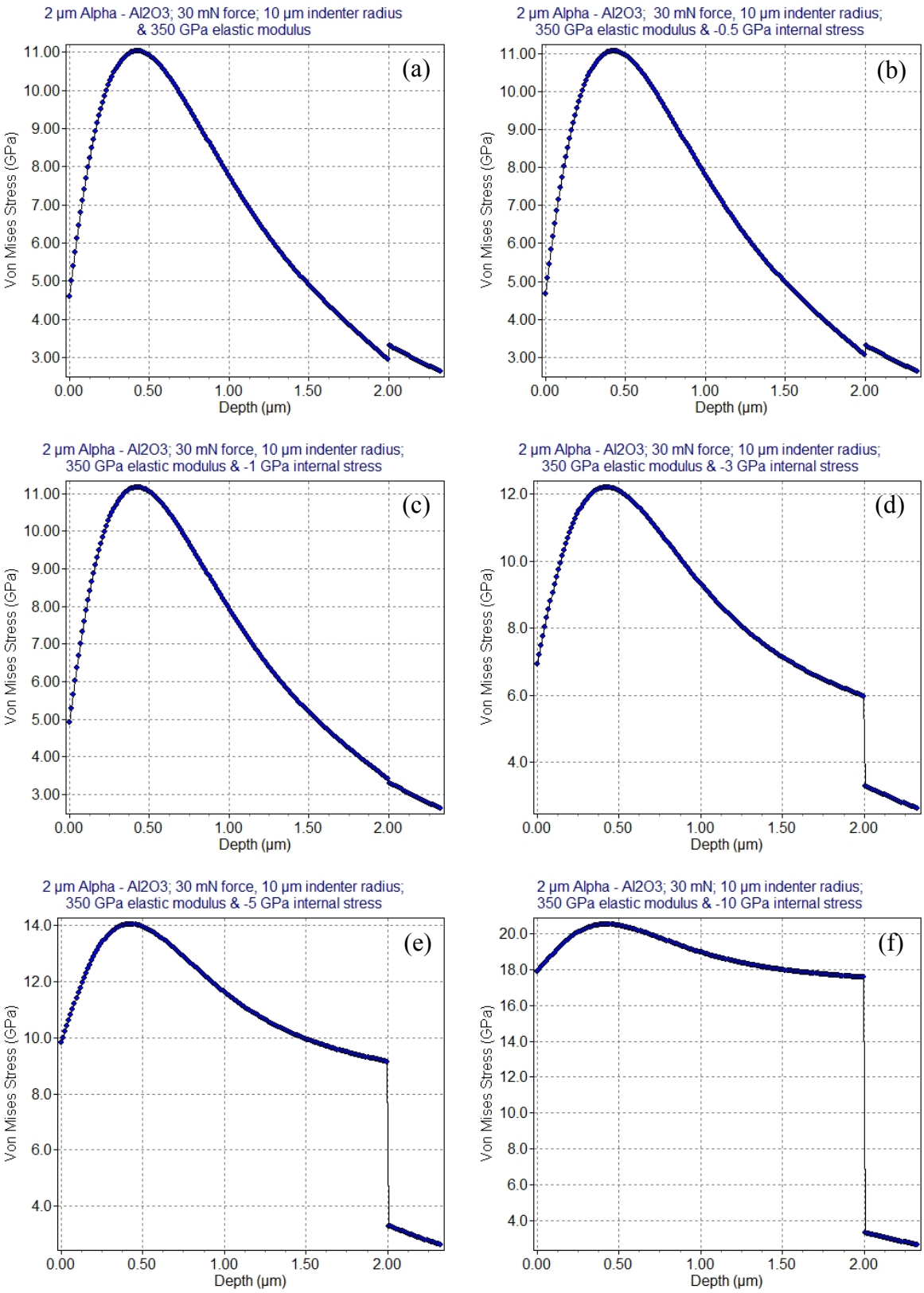

Fig. 4.11: Influence of the residual compressive stress within the α-Al_2O_3 layer on the von Mises stress-depth profile of an α-Al_2O_3 layer on WC-Co substrate. The different modeling parameters, i.e. force, indenter radius, elastic modulus and compressive stress, are summarized in the header of the plots.

At a layer thickness of 2 µm, the steps in the von Mises stress-depth profiles in Figure 4.11 corresponding to the substrate/layer interface can be identified. The first plot (Figure 4.11 (a)) shows the case without compressive stress. In Figure 4.11 (b) a compressive stress of 0.5 GPa is modeled which results in a decrease of the height of the step. It can also be seen, that in both plots the von Mises stress at the onset of the step, i.e. at the interface between the coating and the substrate, is lower than afterwards. In the other four plots in Figure 4.11 the compressive stress increases and, likewise, the height of the step (see also Figure 4.12 (d)) and also the maximum von Mises stress (see Figure 4.12 (a)). The position of the maximum lies within the coating and stays nearly the same in all plots (see Figure 4.12 (b)). Only the curve without compressive stress shows a slightly deeper position (deviations occur only at less then the third decimal digit which is in the sub-nanometer range). In the last four plots in Figure 4.11 (i.e., with 1, 3, 5 and 10 GPa compressive stress) for increasing compressive stress it can be seen that in contrast to the first two (Figures 4.11 (a) and (b)), the von Mises stress at the onset of the step is higher than after the step.

Figure 4.11 (a) shows the stress distribution after coating deposition, where in reality tensile residual stresses occur, which are here assumed as a zero stress level. With increasing compressive stress, the residual stress state goes from tensile to compressive. In blasting investigations done by Holzschuh et al. [20] a residual compressive stress of 7.6 GPa was obtained, which is between the stress levels shown in Figure 4.11 (e) and (f).

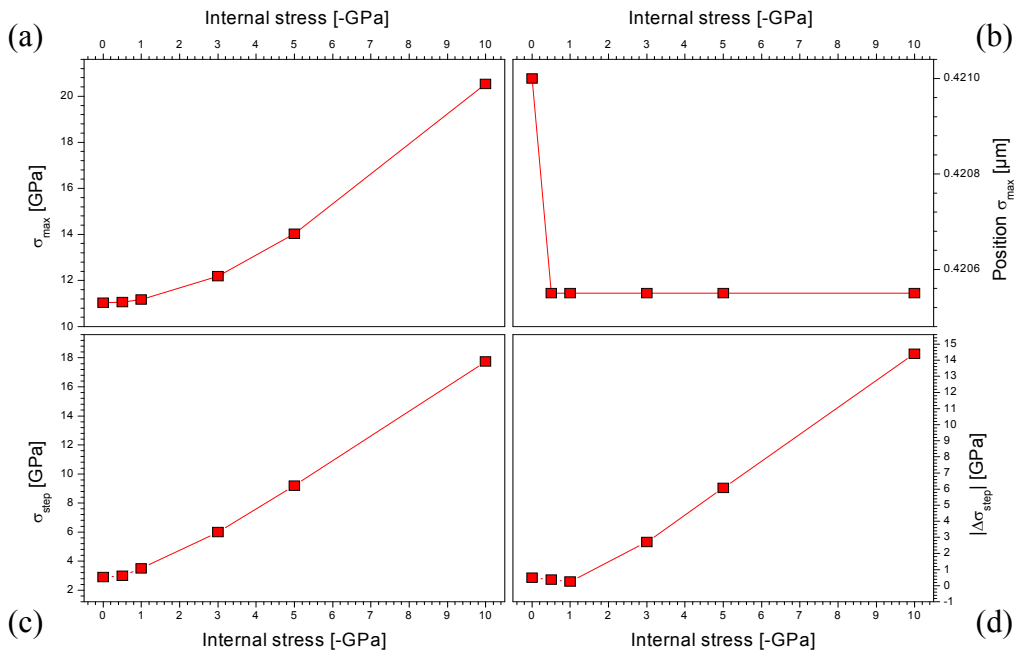

Fig. 4.12: Different parameters, σ_{max} (a), position σ_{max} (b), σ_{step} (c), $|\Delta\ \sigma_{step}|$ (d), obtained for the system WC-Co substrate with an α-Al_2O_3 layer with different residual compressive stresses. It should be noted that the differences in the position of the maximum stress in (b) are in the sub-nanometer range.

Figure 4.12 (c) shows the stress at the onset of the step which increases due to the increasing von Mises stress. The height of the step in Figure 4.12 (d) first decreases from 0 to 1 GPa compressive stress because of the originally acting tensile stress. Afterwards, with increasing compressive stress, an increasing height can be observed.
To predict if the coating is wear resistant and protects the substrate, the yield strength, which indicates the onset of plastic deformation, of both has to be known. In case of Figure 4.11 (b) it can be seen that if the yield strength of the coating exceeds the maximum stress of 11 GPa and the yield strength of the substrate exceeds the maximum stress of 3.4 GPa, the substrate is protected by the thin film and will not be damaged.

Real conditions of force and indenter radius

The same stress investigations on the system WC-Co/ α-Al_2O_3 as before were also made using the real force of 3111 N and an indenter radius of $90*10^3$ µm. The elastic modulus was assumed to be 350 GPa, the layer thickness was 2 µm and the compressive stress was varied between 0 and 10 GPa. Figure 4.13 shows a summary of the six different ELASTICA plots obtained for different compressive stresses.

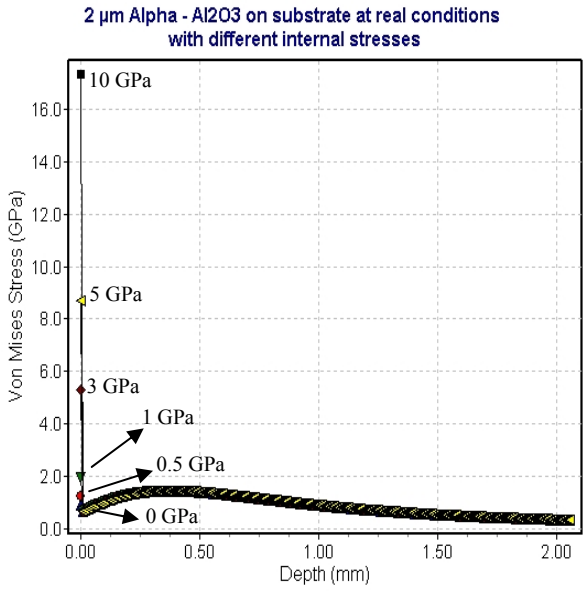

Fig. 4.13: Influence of the residual compressive coating stress on the von Mises stress-depth profile of an α-Al_2O_3 layer on WC-Co substrate at 3111 N force and $90*10^3$ µm indenter radius.

At real conditions the results are very similar to those obtained with the small force and indenter radius. It should be noted that the stress is distributed over a much higher depth compared to the lower force presented in Figure 4.11. The higher the introduced compressive

stress is, the higher is the maximum von Mises stress, as can be seen in Figure 4.13. With increasing von Mises stress, the stress at the onset of the step increases as well. There is also an increase in the height of the step with increasing compressive stress as already shown in Figure 4.12 (d).

In Figure 4.14 the conclusions drawn from Figure 4.13 regarding to the maximum von Mises stress and the position of the maximum are summarized.

As mentioned before, Figure 4.14 (a) shows that the maximum von Mises stress increases with increasing compressive stress. Because of the higher force and indenter radius, which means a smaller contact pressure per unit area, the values of the maximum von Mises stress are lower than in case of the smaller force and indenter radius. Figure 4.14 (b) shows the position of the maximum von Mises stress where the y-axis represents a different scale than in Figure 4.12 (b). It can be seen in Figure 4.13 that there are two relative maxima: Without and in the case of small compressive stress (≤ 0.5 GPa), the relative maximum is located in a depth of about 0.37 mm, which is within the substrate. At higher compressive stress, i.e. 1 up to 10 GPa, the relative maxima is located near the surface within the layer.

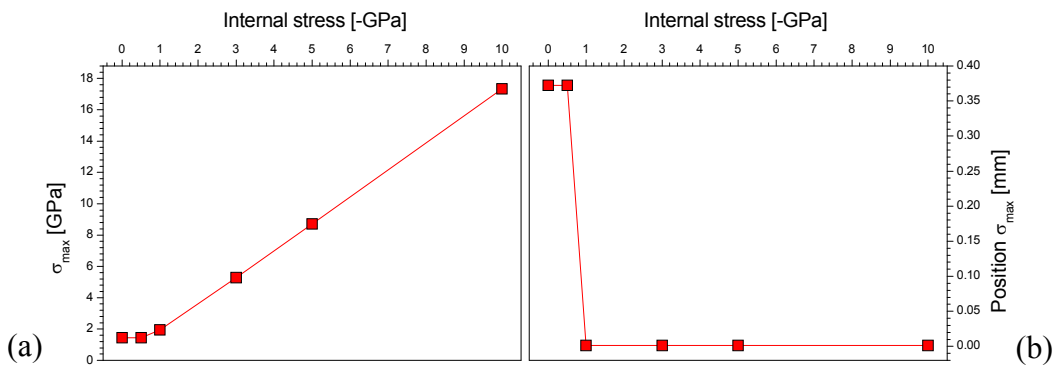

Fig. 4.14: The maximum von Mises stress σ_{max} (a) and the position σ_{max} (b) obtained for the system WC-Co substrate with α-Al_2O_3 layer with different residual compressive coating stresses at real force of 3111 N and indenter radius of $90*10^3$.

4.4 Reduced layer system

As mentioned in the beginning of chapter 4, first ELASTICA investigations lead to reduced layer systems which are three-layer arrangements with WC-Co substrate, a TiCN layer, TiCO as bonding layer and α- or κ-Al_2O_3 on top (see Figure 4.1). The input data for modeling are summarized in Table 4.2. The elastic moduli used are those measured by nanoindentation and the layer thicknesses are about the thickness of a real cemented carbide cutting tool. First, to illuminate if there is a difference between the two different Al_2O_3 polymorphs, each layer was modeled in this three-layer system at different force/indenter radius combinations.

4.4.1 Three layer system with α-Al_2O_3 on top

At first the reduced layer system with α-Al_2O_3 on top was explored. The complete system comprises of the substrate, a 10 µm thick TiCN layer, a 0.4 µm thick TiCO bonding layer and a 5 µm thick α-Al_2O_3 layer on top. The elastic modulus for the WC-Co substrate is 540 GPa. For TiCN, TiCO and α-Al_2O_3, the measured values are 538, 471 and 400 GPa, respectively. The system was modeled at three different force/indenter radius combinations, i.e. 30, 700 and $3111*10^3$ mN force and 10, 500 and $87*10^3$ µm indenter radius, respectively. Figure 4.15 shows the ELASTICA plots for these three combinations. In the reduced layer systems, the indenter radius for the real case is not $90*10^3$ µm as in the hypothetical systems before. Here, an indenter radius of $87*10^3$ µm in case of the α-Al_2O_3 and $84*10^3$ in case of the κ-Al_2O_3 leads to the calculated contact area in chapter 3.2 of about 2.08 mm^2. The difference between the hypothetical and reduced systems can be explained because of the different number of layers and their respective thicknesses. The difference between the two Al_2O_3 polymorphs is due to their different elastic moduli.

In Figure 4.15 (a), the von Mises stress vs. depth plot for the small force of 30 mN and the small indenter radius of 10 µm can be seen. The maximum von Mises stress is found within the α-Al_2O_3 layer. The force and indenter radius are too small to influence the stress state of the other layers and thus no steps at the interfaces can be seen. At the medium force of 700 mN and indenter radius of 500 µm, the von Mises stress depth profile shows a step at each of the three interfaces, as shown in Figure 4.15 (b). Because of the higher force and indenter radius, the maximum von Mises stress shows smaller values as before. The maximum von Mises stress is within the TiCN layer, exactly at the interface between the TiCO and the TiCN layer. The height of the steps is different because of the different elastic moduli. To avoid failure of this coating under these conditions, the yield strength of each layer and the substrate has to be higher than the maxima seen in Figure 4.15 (b). The results of the investigation at real conditions, i.e. 3111 N force and $87*10^3$ µm indenter radius, can be seen in Figure 4.15

(c). The increasing force and indenter radius leads to a decreasing maximum von Mises stress. The scale of the x-axis is in this case in the mm range and the maximum von Mises stress lies within the substrate due to the high force and indenter radius. It can be seen in Figure 4.15, as mentioned earlier, that the higher the force and indenter radius is, the smaller and the deeper positioned in the layer system is the maximum von Mises stress.

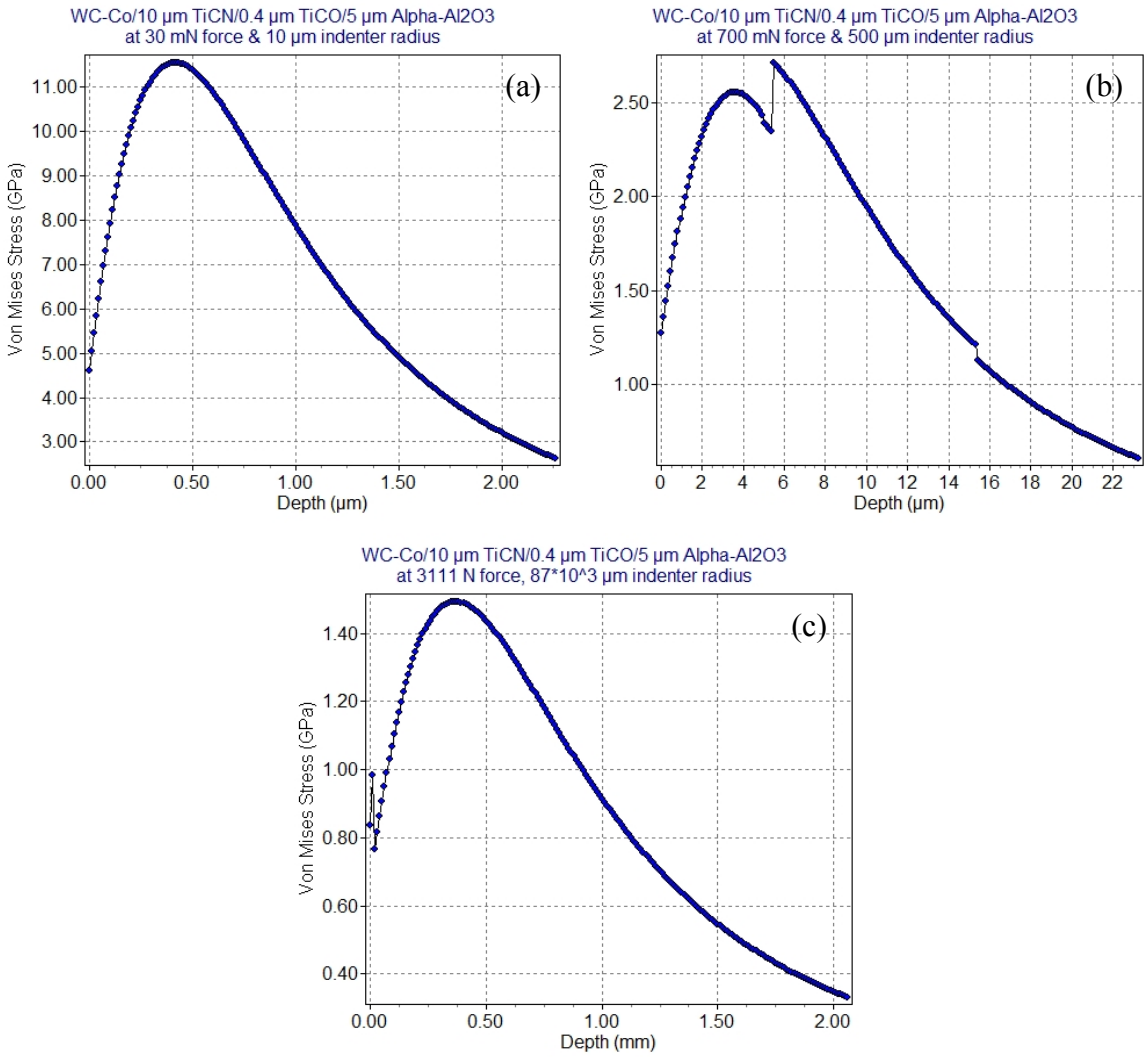

Fig. 4.15: The von Mises stress-depth profile of the reduced layer system with an α-Al_2O_3 layer on top. The different modeling parameters, i.e. layer thickness, force and indenter radius, are summarized in the header of the plots.

4.4.2 Three layer system with κ-Al_2O_3 on top

The same investigations as before were made with κ- instead of α-Al_2O_3. The force/indenter radius combinations are the same, i.e. 30/10, 700/500 and $3111*10^3/87*10^3$ mN or µm, respectively. The elastic modulus of κ-Al_2O_3 is 323 GPa. The layer thicknesses and elastic moduli of the other layers are the same as in section 4.4.1. In Figure 4.16, the von Mises stress-depth profiles of the three different combinations can be seen. As mentioned before, the small force and indenter radius can only influence the stress state at lower depth. Thus, the maximum von Mises stress is within the κ-Al_2O_3 layer and steps at the interfaces can not be observed (see Figure 4.16 (a)).

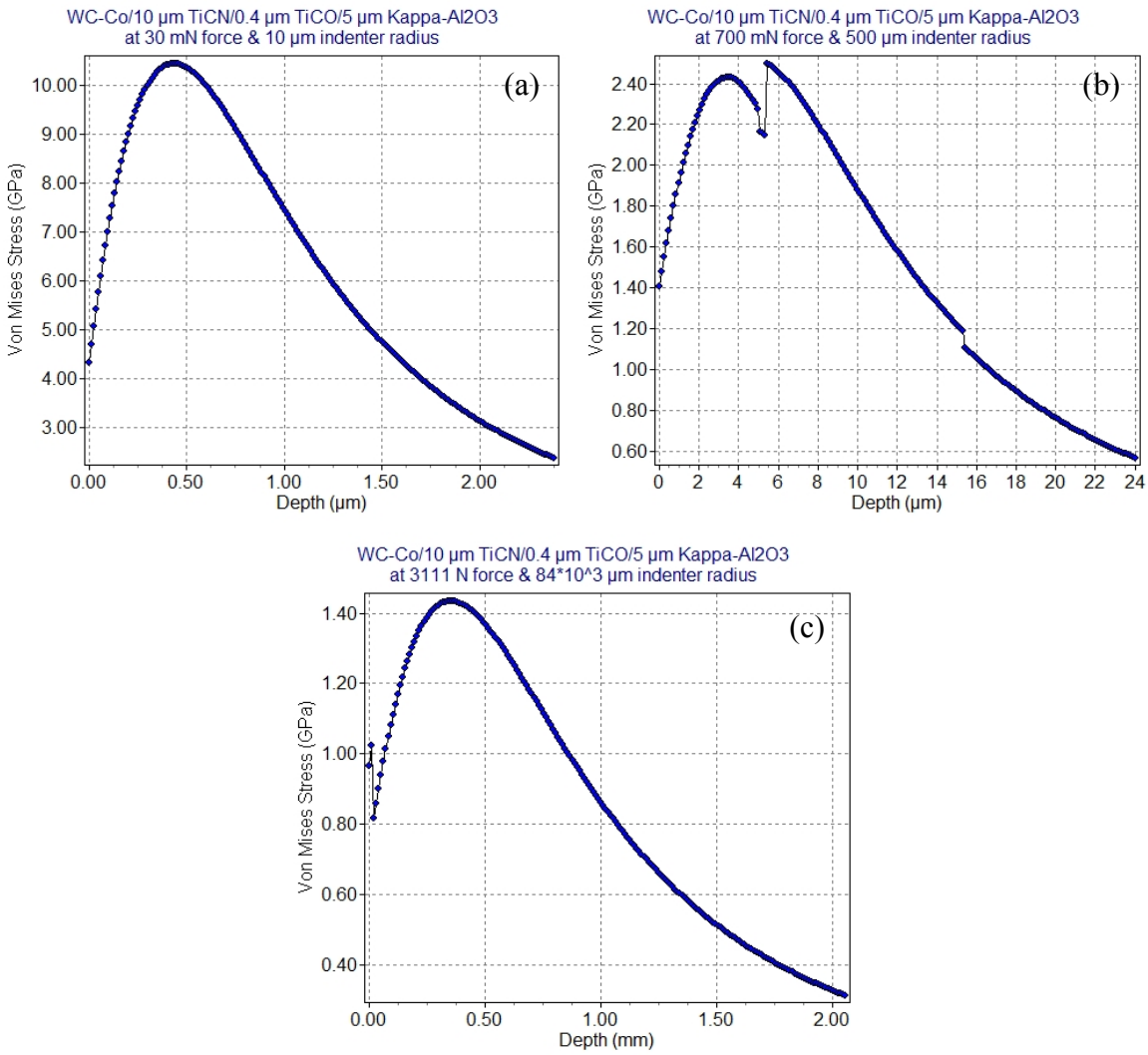

Fig. 4.16: The von Mises stress-depth profile of the reduced layer system with an κ-Al_2O_3 layer on top. The different modeling parameters, i.e. layer thickness, force and indenter radius, are summarized in the header of the plots.

Figure 4.16 (b) shows the ELASTICA plot for the medium force and indenter radius. It looks similar to Figure 4.15 (b) where α-Al_2O_3 is on top. Only the height of the step at the interface between the κ-Al_2O_3 and the TiCO layer is higher than before. The reason is the huger difference between the elastic moduli of κ-Al_2O_3 (323 GPa) and TiCO (471 GPa) compared to α-Al_2O_3 (400 GPa). The maximum von Mises stress is also within the TiCN layer. For real force and indenter radius, the same behavior as before can be observed (see Figure 4.16 (c)). The scale of the x-axis is also in the mm range for these high forces and the maximum von Mises stress is deep within the substrate.

To illuminate the influence of the two different Al_2O_3 polymorphs, the results of the two systems obtained from Figures 4.15 and 4.16 are summarized in Figure 4.17.

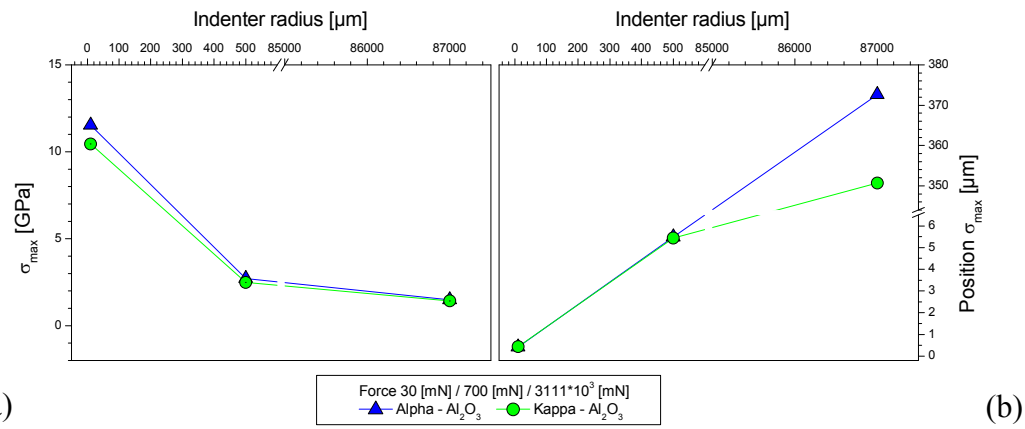

(a) (b)

Fig. 4.17: The maximum von Mises stress σ_{max} (a) and the position σ_{max} (b) obtained for the reduced system with two different Al_2O_3 layers with different force and indenter radius combinations.

Regarding to the maximum von Mises stress, only small deviations can be seen in Figure 4.17 (a) because of the different elastic moduli of the α- and κ-Al_2O_3. The higher elastic modulus of the α-Al_2O_3 phase leads to a higher maximum von Mises stress because of its higher stiffness. With increasing force and indenter radius, the maximum decreases because of the smaller contact pressure per unit area. Figure 4.17 (b) shows the position of the maximum von Mises stress. As mentioned before, the higher the force and indenter radius the more distant is the maximum from the surface. The only significant difference between α- and κ-Al_2O_3 was found for the real force and indenter radius. There, the maximum is within the substrate but in case of α-Al_2O_3 it is deeper in the substrate than in case of κ-Al_2O_3.

4.4.3 Reduced three layer system with internally stressed α-Al_2O_3

Similar investigations as in chapter 4.3.5 regarding to the influence of the internal compressive stresses were done on the reduced three layer system with α-Al_2O_3 on top. The compressive stresses have been varied between 0 and 10 GPa. The input data for modeling, i.e. elastic moduli and layer thickness, are the same as used in chapter 4.4.1. The investigations were done at small force and indenter radius, i.e. 30 mN/10 µm, at medium force and indenter radius, i.e. 700 mN/500 µm, and at real conditions, i.e. 3111 N/87*10^3 µm.

Small force and indenter radius

First internal stress investigations were done at small force of 30 mN and small indenter radius of 10 µm. In Figure 4.18, a summary of the six different ELASTICA von Mises stress versus depth curves obtained for the different compressive stresses can be seen. As mentioned before in chapter 4.4.1, the small force and indenter radius does not effect the stress state at higher distances from the surface. The maximum von Mises stress is in all cases within the α-Al_2O_3 layer and decrease for higher depths. No steps at the interfaces between the layers can be seen. In case of 0, 0.5 and 1 GPa compressive stress, the maximum von Mises stress is nearly the same. At higher compressive stresses, the maximum von Mises stress increases but it is always in the same depth of about 0.42 µm.

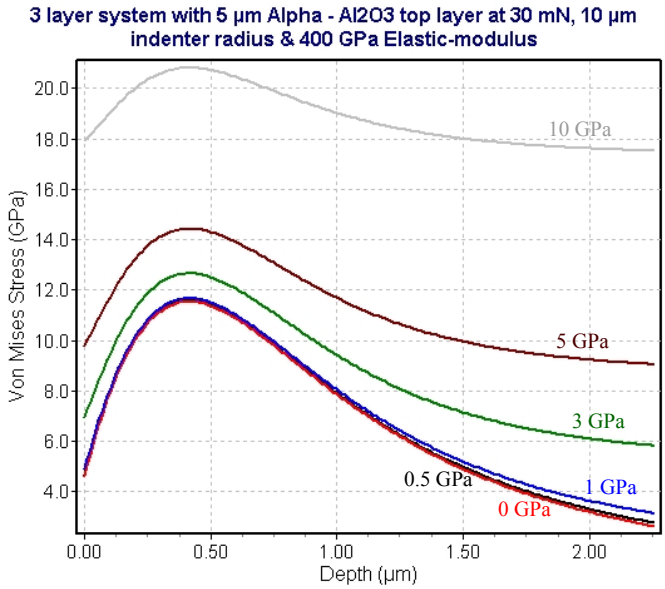

Fig. 4.18: Influence of the residual compressive stress within the α-Al_2O_3 layer on the von Mises stress-depth profile of the reduced layer system at 30 mN force and 10 µm indenter radius.

Medium force and indenter radius

Investigations regarding the internal compressive stress were also done for a moderate force of 700 mN and an indenter radius of 500 µm. Figure 4.19 shows the six ELASTICA plots obtained for the different compressive stress levels, i.e. from 0 up to 10 GPa. At this force/indenter radius combination, the steps in the von Mises stress-depth profile corresponding to the different interfaces between the layers can be identified. Figure 4.19 (a) shows the stress distribution after coating deposition, where in reality tensile residual stresses occur [20] which are here assumed as zero stress level.

In Figure 4.19 (b), a compressive stress of 0.5 GPa is assumed which results in an increase of the height of the step at the interface between the α-Al_2O_3 and the TiCO layer. The maximum von Mises stress is as in Figure 4.19 (a) within the TiCN layer. At higher compressive stresses beginning at 1 GPa, (see Figure 4.19 (c)) the position of the maximum von Mises stress is within the α-Al_2O_3 layer. The higher the compressive stress is, the higher is the von Mises stress (see Figure 4.19 (b) to (f)). With increasing compressive stresses also the height of the step at the interface between the α-Al_2O_3 and the TiCO layer increases while the steps at the other interfaces decrease.

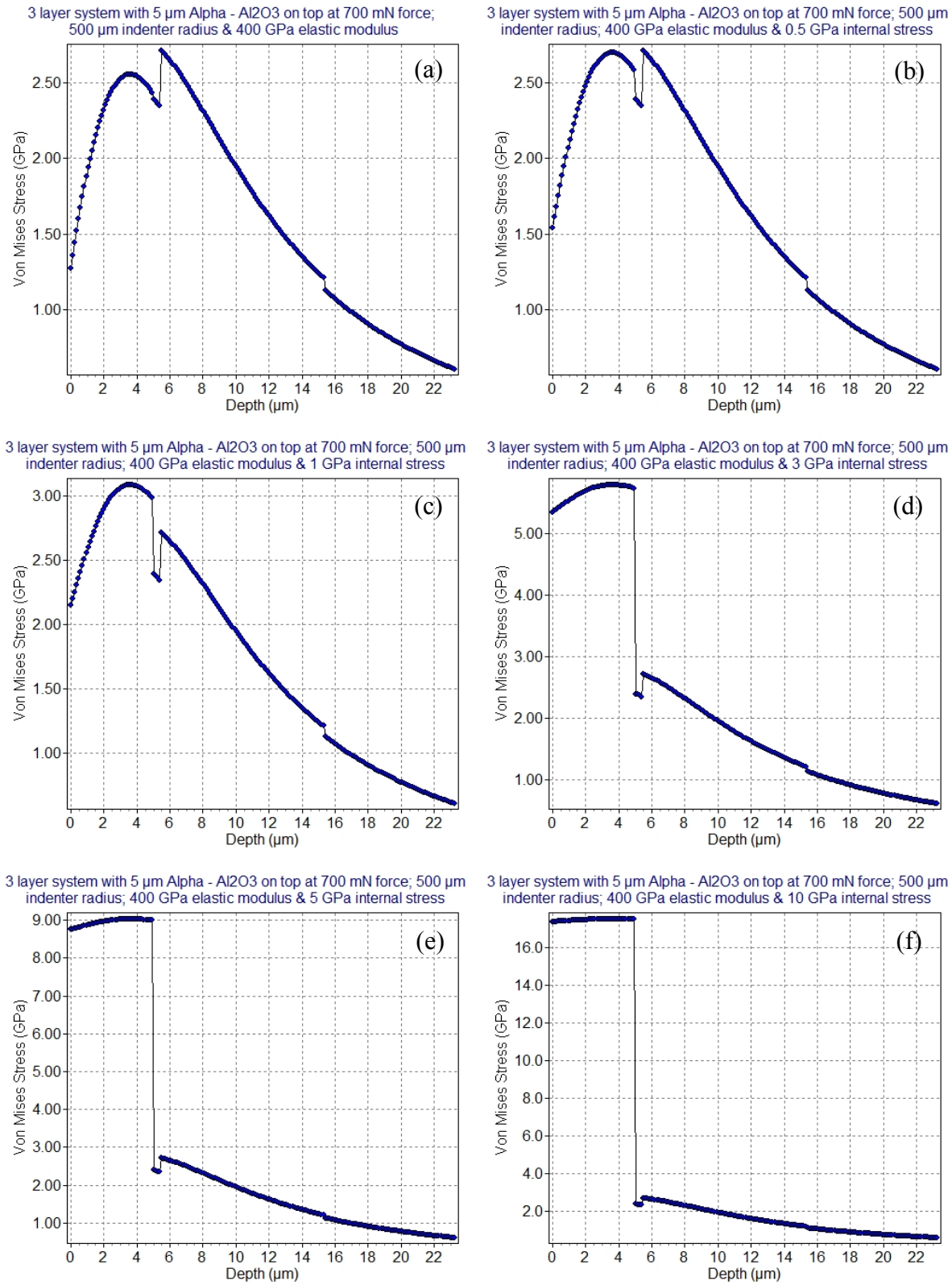

Fig. 4.19: Influence of the residual compressive stress within the α-Al_2O_3 layer on the von Mises stress-depth profile of the reduced system with an α-Al_2O_3 layer on top. The different modeling parameters, i.e. force, indenter radius, elastic modulus and compressive stress are summarized in the header of the plots.

In Figure 4.20 the results regarding the maximum von Mises stress (Figure 4.20 (a)) and the position of the maximum (Figure 4.20 (b)) of the reduced layer system at small and medium force and indenter radius are summarized. The difference in the maximum von Mises stress is due to the smaller contact pressure per unit area in case of the higher force and indenter radius which leads to a smaller von Mises stress (see Figure 4.20 (a)). The higher the force and indenter radius is, the deeper within the layer system is the maximum located, as can be seen in Figure 4.20 (b). As mentioned above for higher force and indenter radius, the maximum lies in case of 0 and 0.5 GPa compressive stress within the TiCN layer and at higher compressive stresses within the α-Al_2O_3 layer. This means that at given loading conditions, the compressive stresses in the top layer can be used to shift the stress maximum due to the mechanical loading between different layers.

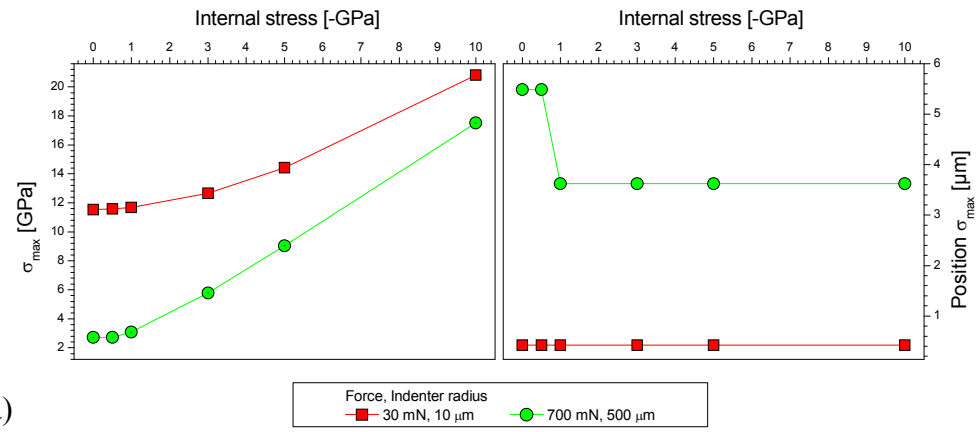

(a) (b)

Fig. 4.20: The maximum von Mises stress σ_{max} (a) and the position σ_{max} (b) obtained for the reduced system with α-Al_2O_3 on top with different residual compressive stresses at small (30 mN/10 µm) and medium (700 mN/500 µm) force and indenter radius.

Real conditions of force and indenter radius

The same investigations were also made for real conditions, i.e. 3111 N force and $87*10^3$ µm indenter radius. In Figure 4.21, the summary of the six ELASTICA curves obtained for the different compressive stresses can be seen.

The results are very similar to those obtained for the hypothetical one layer system with an α-Al_2O_3 layer on the WC-Co substrate (see Figure 4.13). An increasing compressive stress results in an increasing maximum von Mises stress and also in an increase in the height of the step at the interfaces. The stress is, compared to the small and medium force and indenter radius, distributed over a much higher depth which lies in the mm range (see the x-axis in Figure 4.21). Figure 4.22 shows the conclusions drawn from Figure 4.21 regarding to the maximum von Mises stress and its position.

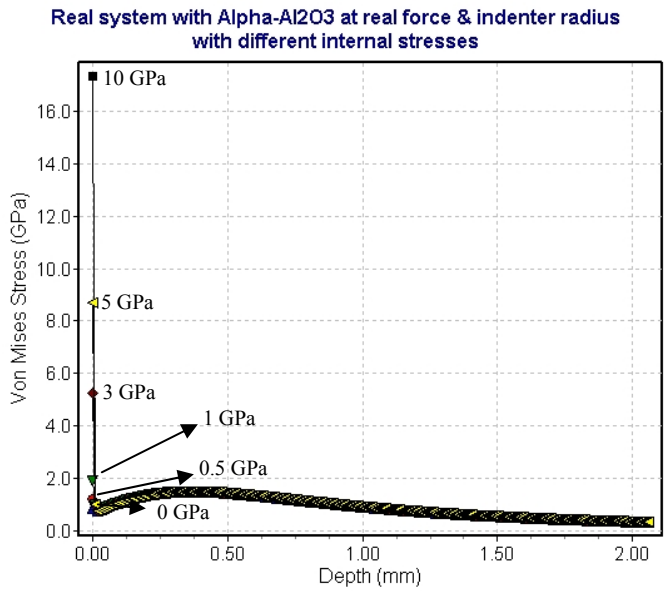

Fig. 4.21: Influence of the residual compressive stress within the α-Al_2O_3 layer on the von Mises stress-depth profile of the reduced layer system at 3111 N force and $87*10^3$ µm indenter radius.

Figure 4.22 (a) shows the already mentioned increase of the maximum von Mises stress with increasing compressive stress, whereas Figure 4.22 (b) gives the position of the maximum von Mises stress. Figure 4.21 shows the same behavior as it can be seen in Figure 4.13 in case of the hypothetical layer, where two relative maxima can be observed. Without and in case of 0.5 GPa compressive stress, the relative maximum is located within the substrate. From 1 up to 10 GPa compressive stress, the maximum is located near the surface of the α-Al_2O_3 layer (see Figure 4.22 (b)).

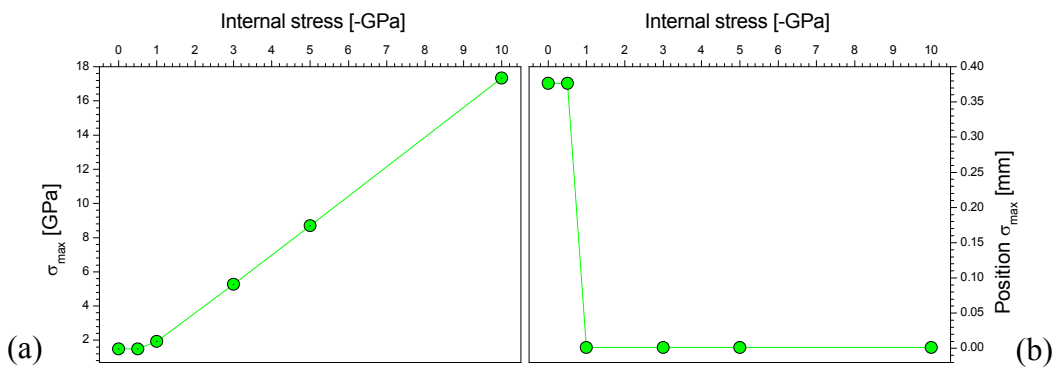

Fig. 4.22: The maximum von Mises stress σ_{max} (a) and the position σ_{max} (b) obtained for the reduced layer system with α-Al_2O_3 on top with different residual compressive stresses at real force of 3111 N and indenter radius of $87*10^3$.

5 Summary, conclusions and outlook

5.1 Summary

The purpose of this work was to find a strategy for optimizing CVD layered thin film coatings on cemented carbide cutting tools with respect to their mechanical failure. The approach used is based on a combination of indentation experiments, to determine the mechanical properties, i.e. elastic modulus and hardness of the coatings, and the commercial analytical simulation package ELASTICA, to calculate the stress imposed by external mechanical loads within the individual layers. There, the von Mises comparison stress is the most important stress criterion for the onset of plastic deformation and thus, for the estimation of the load carrying capacity of coated systems. First investigations were made on the uncoated WC-Co substrate, whereas the investigations of the coating systems were divided in two parts: first, hypothetical layer systems which are one-layer coatings of a particular layer (TiN, TiCN, α- and κ-Al_2O_3) on the WC-Co substrate, have been explored. The second part is focused on three-layered reduced systems which are very similar to a real coating system on a cemented carbide cutting tool. They comprise of the WC-Co substrate, a TiCN base layer, a TiCO bonding layer and α- or κ-Al_2O_3 as top layer.
The simulations were done under particular load and indenter radius situations, i.e. at small force of 30 mN and indenter radius of 10 µm, medium force of 700 mN and indenter radius of 500 µm and at real conditions derived from cutting tests with a force of 3111 N and an indenter radius of about $90*10^3$ µm. Some investigations where also done with internal compressive stress ranging from 0 to 10 GPa.

WC-Co substrate

For constant indenter radius it was found that the higher the force is, the higher and the deeper within the layer system the maximum of the von Mises stress can be found. By varying the indenter radius, combinations of high force and indenter radius result in a smaller maximum von Mises stress due to the smaller contact pressure per unit area, and in a deeper position of the maximum.

Hypothetical layer system

The results obtained of these investigations are very similar to the substrate. The higher force and indenter radius leads to a smaller von Mises stress, and the maximum moves deeper into

the layer system. At the interfaces between the different layers and the substrate, steps can be obtained because of the difference of the respective elastic moduli. A higher elastic modulus means a stiffer material, and the stiffer the material is, the higher is the von Mises stress and the deeper within the layer-substrate system is the position of the maximum. The layer thickness affects the von Mises stress versus depth curves only for huge differences between the elastic moduli of the substrate and the layer. A substrate which is stiffer than the layer supports a thinner layer more than a thicker one, i.e. there a thinner layer could seem to be stiffer resulting in a higher von Mises stress. The two different Al_2O_3 polymorphs show only small deviations due to their different elastic moduli. With increasing compressive stress within the α-Al_2O_3 layer the maximum von Mises stress under an indent increases as well, whereas the position of the maximum is in all cases in the same depth. Applying real conditions, the von Mises stress is smaller, and it is distributed over a much higher depth compared to the lower force.

Reduced layer system

The von Mises stress versus depth curves for both the α- and the κ-Al_2O_3 are very similar; only regarding to the maximum von Mises stress and the height of the step at the interface between the respective Al_2O_3 and the TiCO bonding layer, small deviations because of the different elastic moduli of α- and κ-Al_2O_3 can be observed. The higher elastic modulus of α-Al_2O_3 results in a higher maximum von Mises stress and a smaller step at the interface between α-Al_2O_3 and TiCO. The latter is related to the smaller difference of the elastic moduli between α-Al_2O_3 and TiCO compared to κ-Al_2O_3. Also for the reduced system with α-Al_2O_3, an increase of the von Mises stress with increasing compressive stress was found. For the medium force and indenter radius, where steps at the interfaces can be observed, also an increase of the step at the interface between the α-Al_2O_3 and TiCO layers with increasing compressive stresses was found, whereas the steps at the other interfaces decrease. The position of the maximum von Mises stress is in all cases at the interface between the α- Al_2O_3 and the TiCO layer except in case of 0 and 0.5 GPa compressive stress, where it is within the α-Al_2O_3 layer. The investigations at real conditions show the results comparable to those obtained for the hypothetical system with α-Al_2O_3.

5.2 Conclusions

Within this thesis it has been demonstrated that with a simulation program like ELASTICA the following information can be obtained:

1. It is possible to illuminate the stress distribution in the layer system for different contact situations.

2. From the von Mises stress versus depth curves, information on the level and the position of the maximum stress can be derived. It can be assumed that huge levels of von Mises stresses at interfaces of layers and substrate are crucial and can lead to early failure of the coating, because of the arising interfacial shear stresses.
3. By varying the layer thickness, the elastic modulus or the internal stresses, it is possible to move high stress levels to less crucial positions.

5.3 Outlook

Experimental

Based on the experience gained within this thesis, the following two comments related to the experimental work are important for the future. The first one is related to the measurement of the elastic modulus and hardness by nanoindentation which is a sophisticated measurement with many sources of error if not done correctly. The second comment is related to the measurement of the stresses by XRD, where it is necessary to have exact values of the stress state and also the distribution within the coating. Having correct data of these material properties is essential for valid modeling efforts.

Modeling

As already pointed out, the validity of the modeling approaches is based on the availability of as much as possible exact values for the different material properties. Data like the yield strength of the substrate and the coating materials are necessary to make predictions if the coating is wear resistant and protects the substrate. Further investigations regarding to the influence of the different layer thicknesses, particularly in the three-layered systems, should be done. It is also recommended to do additional investigations with other simulation programs, e.g. the Film Doctor software, where a huge variety of contact and load situations with more than three layers can be modeled. Effects of other input parameters like structure, roughness, intrinsic stresses as well as material defects and inclusions can be taken into account. Furthermore, to develop a feeling how valid the simulation results are, the different coatings should be synthesized and evaluated by different tribological and cutting tests.

6 References

[1] J. Eller: 'Optimal Layer Design', Bachelorarbeit, Chemnitz University of Technology, 2003

[2] T. Chudoba, N. Schwarzer, F. Richter, 'Steps towards a mechanical modeling of layered systems', Surface and Coatings Technology 154 (2002) 140-151.

[3] K.J.A. Brookes, 'Half a century of hardmetals', Metal Powder Report 50 (1995) 22-28.

[4] K.L. Choy, 'Chemical vapour deposition of coatings', Progress in Materials Science 48 (2003) 57-170.

[5] S. Ruppi, 'Advances in chemically vapour deposited wear resistant coatings', Journal De Physique IV 11 (2001) 847-859.

[6] H. Holleck, 'Material selection of hard coatings', Journal of Vacuum Science & Technology 4 (1986) 2661-2669.

[7] S. Vuorinen, R.H. Hoel, 'Interfacial characterization of chemically vapor-deposited titanium carbide on cemented carbide', Thin Solid Films 232 (1993) 73-82.

[8] H.O. Pierson: 'Handbook of Chemical Vapor Deposition', 2nd ed., Noyes Publications, New Jersey, 1999.

[9] F.W. Bach, K. Möhwald, T. Wenz: 'Moderne Beschichtungsverfahren', 2nd ed., Wiley-VCH, Weinheim, 2005, p. 71-93.

[10] A. Larsson, S. Ruppi, 'Microstructure and properties of Ti(C,N) coatings produced by moderate temperature chemical vapour deposition', Thin Solid Films 402 (2002) 203-210.

[11] S. Ruppi, A. Larsson, A. Flink, 'Nanoindentation hardness, texture and microstructure of α-Al_2O_3 and κ-Al_2O_3 coatings', Thin Solid Films 516 (2008) 5959-5966.

[12] S. Ruppi, 'Deposition, microstructure and properties of texture-controlled CVD α-Al_2O_3 coatings', International Journal of Refractory Metals & Hard Materials 23 (2005) 306-316.

[13] D.T. Quinto, 'Mechanical property and structure relationships in hard coatings for cutting tools', Journal of Vacuum Science & Technology A 6 (1988) 2149-2157.

[14] I.C. Noyan, J.B. Cohen: 'Residual Stress - Measurement by Diffraction and Interpretation'. Springer, New York, 1987, p. 276.

[15] M. Birkholz: 'Thin Film Analysis by X-Ray Scattering'. Wiley-VCH, Weinheim, 2006, p. 355.

[16] C. Barbatti, J. Garcia, R. Pitonak, H. Pinto, A. Kostka, A. Di Prinzio, M.H. Staia, A.R. Pyzalla, 'Influence of micro-blasting on the microstructure and residual stresses of CVD κ-Al_2O_3 coatings', Surface and Coatings Technology 203 (2009) 3708-3717.

[17] A.J. Perry, J.A. Sue, P.J. Martin, 'Practical measurement of the residual stress in coatings', Surface and Coatings Technology 81 (1996) 17-28.

[18] Ceratizit Luxembourg, Personal communication, April 2010.

[19] B.D. Cullity: 'Element of X-ray diffraction', 2nd ed., ADDISON-Wesley, 1978, p. 555.

[20] H. Holzschuh, M. Klaus, C. Genzel: 'Influence of the residual stress state on the thoughness of CVD coated cemented carbide cutting tools', *Advances in Powder Metallurgy & Particulate Materials*. 2008. Washington D.C.

[21] A.C. Fischer-Cripps: 'Nanoindentation', 2nd ed., Springer-Verlag, New York, 2004.

[22] A.C. Fischer-Cripps: 'Introduction to Contact Mechanics', 2nd ed., Springer, New York, 2007.

[23] W.C. Oliver, G.M. Pharr, 'Improved technique for determining hardness and elastic modulus using load and displacement sensing indentation experiments', Journal of Materials Research 7 (1992) 1564-1580.

[24] T. Chudoba, 'Measurement of hardness and young´s modulus by nanoindentation', in A. Cavaleiro and J.T.M. De Hosson (eds.), 'Nanostructured Coatings', 2006, Springer, New York.

[25] A.C. Fischer-Cripps, 'Critical review of analysis and interpretation of nanoindentation test data', Surface and Coatings Technology 200 (2006) 4153-4165.

[26] ASMEC, http://www.asmec.de/d.htm, April 2010.

[27] SIOMEC, http://www.siomec.de/Frames.aspx?page=Elastica.aspx, April 2010.

[28] J.-J. Milan, "Pression de Hertz", http://de.wikipedia.org/w/index.php?title=Datei:Hertz.png&filetimestamp=20041111213711, April 2010.

[29] N. Schwarzer, F. Richter, G. Hecht, 'The elastic field in a coated half-space under Hertzian pressure distribution', Surface and Coatings Technology 114 (1999) 292-303.

[30] O. Wänstrand, N. Schwarzer, T. Chudoba, A. Kassman-Rudolphi, 'Load carrying capacity of Ni plated media in spherical indentation: Experimental and theoretical results', Surface Engineering 18 (2002) 98-104.

[31] C. Walter, C. Mitterer, '3D versus 2D finite element simulation of the effect of surface roughness on nanoindentation of hard coatings', Surface and Coatings Technology 203 (2009) 3286-3290.

[32] KYOCERA, http://www.kyocera.eu/content/pool/eu/en/cutting_tools/news/2005/high-performance_cutting.-cps-9873-Image.cpsarticle.jpg, April 2010.

[33] Wikimedia, "Kontakt Kugel-Ebene", http://upload.wikimedia.org/wikipedia/commons/4/41/Kontakt_Kugel_Ebene.jpg, April 2010.

[34] K. Kutschej, B. Rashkova, J. Shen, D. Edwards, C. Mitterer, G. Dehm, 'Experimental studies on epitaxially grown TiN and VN films', Thin Solid Films 516 (2007) 369-373.

[35] C. Kral, W. Lengauer, D. Rafaja, P. Ettmayer, 'Critical review on the elastic properties of transition metal carbides, nitrides and carbonitrides', Journal of Alloys and Compounds 265 (1998) 215-233.

[36] Ceratizit Austria, Schnittkraftauswertung auf V960, 1996.

[37] D. Hochauer, C. Mitterer, M. Penoy, C. Michotte, H.P. Martinz, M. Kathrein, 'Titanium doped CVD alumina coatings', Surface and Coatings Technology 203 (2008) 350-356.

[38] G.A. Fontalvo, R. Daniel, C. Mitterer, 'Interlayer thickness influence on the tribological response of bi-layer coatings', Tribology International 43 108-112.